

Steepening mass profiles, dark matter and environment of X-ray bright elliptical galaxies

Payel Das^{1*}, Ortwin Gerhard¹, Eugene Churazov^{2,3}, Irina Zhuravleva²

¹ *MPI für Extraterrestrische Physik, P.O. Box 1603, 85740 Garching, Germany*

² *MPI für Astrophysik, Karl-Schwarzschild-Strasse 1, 85741 Garching, Germany*

³ *Space Research Institute (IKI), Profsoyuznaya 84/32, Moscow 117810, Russia*

Accepted 2010 July 25. Received 2010 July 19; in original form 2010 April 29

ABSTRACT

We use a new non-parametric Bayesian approach to obtain the most probable mass distributions and circular velocity curves along with their confidence ranges, given deprojected density and temperature profiles of the hot gas surrounding X-ray bright elliptical galaxies. For a sample of six X-ray bright ellipticals, we find that all circular velocity curves are rising in the outer parts due to a combination of a rising temperature profile and a logarithmic pressure gradient that increases in magnitude. Therefore at large radii, mass density profiles rise more steeply than isothermal profiles, implying that we are probing the more massive group-sized haloes in which these galaxies are embedded. Comparing the circular velocity curves we obtain from X-rays to those obtained from dynamical models, we find that the former are often lower in the central ~ 10 kpc. This is probably due to a combination of: i) Non-thermal contributions of up to $\sim 35\%$ in the pressure (with stronger effects in NGC 4486), ii) multiple-temperature components in the hot gas, iii) incomplete kinematic spatial coverage in the dynamical models, and iv) mass profiles that are insufficiently general in the dynamical modelling. Complementing the total mass information from the X-rays with photometry and stellar population models to infer the dark matter content, we find evidence for massive dark matter haloes with dark matter mass fractions of $\sim 35\text{--}80\%$ at $2R_e$, rising to a maximum of $80\text{--}90\%$ at the outermost radii. We also find that the six galaxies follow a Tully-Fisher relation with slope ~ 4 and that their circular velocities at $1R_e$ correlate strongly with the velocity dispersion of the local environment. As a result, the galaxy luminosity at $1R_e$ also correlates with the velocity dispersion of the environment. These relations suggest a close link between the properties of central X-ray bright elliptical galaxies and their environments.

Key words: galaxies: elliptical and lenticular, CD – galaxies: evolution – X-rays: galaxies – galaxies: stellar content – dark matter

1 INTRODUCTION

X-ray bright elliptical galaxies are massive galaxies, thought to be among the most evolved systems in our Universe with a complex formation history. They are believed to grow from mergers between smaller galaxies, and after star formation ceases at $z \sim 1\text{--}2$, they become larger and less compact through the significant accretion of stellar material from neighbouring smaller systems (e.g. van Dokkum et al. 2008; Naab et al. 2009).

Knowledge of the total mass distributions of galaxies gives us insight into their formation history at several different levels. At the most basic level, it tells us the combined

mass of these collapsed systems. If we incorporate information from photometry and stellar population models, we can disentangle the respective luminous and dark matter components. Comparing their properties with what is expected from simulations will help place constraints on current theories of galaxy evolution. The mass profile could also be used as input in dynamical models of galaxies, therefore mitigating the usual mass-anisotropy degeneracy. This would provide more stringent constraints on the orbital structure, which serves as an imprint of the processes that occurred in the past to create the galaxy. Finally, it will give us an insight into the relations between the masses of collapsed systems and the environments they reside in.

There are several methods in the literature for obtaining the mass distributions of elliptical galaxies. Dy-

* E-mail: pdas@mpe.mpg.de

Galaxy (1)	Classification (2)	Distance (Mpc) (3)	$\log L_X$ (4)	σ_{env} (5)	Source (6)
NGC 1399	cD; E1 pec	19.95	41.63	370	D01
NGC 1407	E0	28.84	41.00	387	T06
NGC 4472	E2	16.29	41.43	607	G99
NGC 4486	E0-E1 pec	16.07	42.95	762	G99
NGC 4649	E2	16.83	41.28	702	G99
NGC 5846	E0-E1	24.20	41.65	322	M05

Table 1. Sample of X-ray bright elliptical galaxies: (1) Galaxy name, (2) galaxy classification from NED, (3) distance taken from Tonry et al. (2001), (4) X-ray luminosity taken from O’Sullivan et al. (2001), (5) velocity dispersion of the surrounding environment and (6) source of the velocity dispersion values. References are D01 (Drinkwater et al. 2001), T06 (Trentham et al. 2006), G99 (Gavazzi et al. 1999), M05 (Mahdavi et al. 2005).

namical models can be constructed by superposing a library of orbits (e.g. Rix et al. 1997; Gebhardt et al. 2003; Thomas et al. 2004; Cappellari et al. 2006) or distribution functions (e.g. Dejonghe et al. 1996; Gerhard et al. 1998; Kronawitter et al. 2000), or by constructing a system of particles (de Lorenzi et al. 2008, 2009) such that the projection of the system best reproduces observed surface-brightness and kinematic profiles. These models give the mass distribution and orbital structure of the galaxies simultaneously. Strong lensing gives the projected mass within the Einstein ring and weak lensing studies provide mass density profiles for a sample of galaxies (e.g. Treu & Koopmans 2004; Mandelbaum et al. 2006; Gavazzi et al. 2007; Koopmans et al. 2009). The properties of X-ray bright elliptical galaxies allow an additional possibility for obtaining mass distributions (e.g. Nulsen & Böhringer 1995; Fukazawa et al. 2006; Churazov et al. 2008; Nagino & Matsushita 2009). The X-ray spectra are dominated by lines and by continuous emission from thermal bremsstrahlung radiation produced in the surrounding halo of hot gas. The spectra can be deprojected and fitted to derive 3-D temperature and density profiles of the gas, and if we assume it is in hydrostatic equilibrium, we can derive the enclosed mass profile.

Generally the literature points towards isothermal mass distributions in elliptical galaxies, with a conspiracy between the luminous and dark matter components resulting in flat circular velocity curves similar to that found in spiral galaxies (e.g. Kronawitter et al. 2000; Koopmans et al. 2009; Churazov et al. 2010). Fukazawa et al. (2006) however, determined mass distributions of a sample of 53 elliptical galaxies from Chandra and XMM-Newton observations, and found that they are better described by power laws with an index $\gtrsim 1$, i.e. their circular velocity curves range between flat and rising. The particle-based dynamical models of de Lorenzi et al. (2008, 2009) found falling circular velocity curves for the intermediate-luminosity galaxies, NGC 3379 and NGC 4697. Thomas et al. (2007) found a range of slopes in the elliptical galaxies belonging to the Coma cluster, from their orbit-based dynamical models.

In this paper, we examine the isothermality of mass distributions from X-ray observations and whether they are accurate enough to derive dark matter mass profiles, use in dynamical modelling, and determine global properties of elliptical galaxies. To address these issues we need to apply

hydrostatic equilibrium using a procedure that is as free from systematic biases as possible.

Cowie et al. (1987); Humphrey et al. (2006); Fukazawa et al. (2006); Nagino & Matsushita (2009) used methods where the measured temperature and density profiles are parameterised before applying hydrostatic equilibrium, to circumvent differentiating the observed profiles, which are often noisy. Churazov et al. (2008) avoided differentiation by interpolating to obtain only the potential profile. Nulsen & Böhringer (1995) found the most likely mass profile of NGC 4486 (M87) from temperature and density profiles using a non-parametric method, and Humphrey et al. (2009) used a parametric Bayesian analysis. The parametric methods used in the literature will generally underestimate the range of mass profiles consistent with the data. They also introduce systematic biases in the masses derived because of the assumptions on the profile shapes.

We use the sample of galaxies from Churazov et al. (2010) and we discuss them and the properties of the hot X-ray gas they harbour briefly in Section 2. In Section 3 we describe the implementation of a new non-parametric Bayesian approach to obtain the total mass and circular velocity profiles from hydrostatic equilibrium. In Section 4 we show the results of tests of the new method and how to optimise it. In Section 5 we show the total mass profiles and circular velocity curves we obtain by applying the method to the sample of galaxies, and the stellar and dark matter contributions we infer from published photometry and stellar population model mass-to-light ratios. In Section 6 we compare the individual circular velocity curves we obtain to previous determinations from X-rays and published dynamical models. We also examine the isothermality of the mass profiles of these galaxies, and look for any correlations that may exist between the stellar component, the total circular velocities and properties of the surrounding environment. We end with our conclusions in Section 7.

2 THE SAMPLE

We work on the sample of galaxies analysed in Churazov et al. (2010). Table 1 lists the galaxies in the sample, the galaxy classification, the distances we assume, the X-ray luminosity and the velocity dispersion of the surrounding environment. NGC 1399 is located at the centre of the Fornax cluster, NGC 1407 and NGC 5846 at the centre of

groups, and NGC 4472, NGC 4486 and NGC 4649 at the centre of sub-clumps in the irregular Virgo cluster. NGC 4486 is at the centre of the most massive sub-component. Drinkwater et al. (2001) determined the velocity dispersion of the environment surrounding NGC 1399 from 92 galaxies within a radius of about 2.7° (930 Mpc), Trentham et al. (2006) from 35 galaxies within about 900 kpc of NGC 1407 and Mahdavi et al. (2005) from 87 galaxies within a radius of 1.8° (777 kpc) of NGC 5846. Gavazzi et al. (1999) calculated the velocity dispersion in sub-clumps containing NGC 4472, NGC 4486 and NGC 4649 using 166, 62 and 58 galaxies respectively.

The sample galaxies harbour significant amounts of hot gas that except in the case of NGC 4486, appears relatively undisturbed, suggesting hydrostatic equilibrium.

2.1 Density and temperature profiles of the hot gas

The X-ray spectrum of the hot gas surrounding X-ray bright ellipticals consists of many emission lines and continuous emission primarily from the mechanism of thermal bremsstrahlung. To obtain information on the temperature and density profiles of the gas, the spectra are fitted with models that make assumptions about the absorption along the line-of-sight and the metal abundance in the gas.

We use the deprojected temperature and density profiles obtained by Churazov et al. (2010) from Chandra and XMM-Newton observations, shown in Figure 1. The composite profiles benefit in the central region from the high spatial resolution of Chandra and in the outer parts from the large field-of-view and collecting power of XMM-Newton. The XMM-Newton profiles are not more spatially extended than the Chandra profiles as one would normally expect, because several pointings were used with the Chandra instrument.

Churazov et al. first spherically deprojected the X-ray spectra using a non-parametric least-squares algorithm described in Churazov et al. (2003). This finds the set of 3-D spectra in spherical shells that project to best-fit the observed spectra, assuming a power-law decline in the emission outside the maximum observed radius. The deprojected spectra were then fit with the single-temperature APEC code in XSPEC, which resulted in a determination of the 3-D temperature and density for each shell. The abundance of heavy elements in the model was fixed at 0.5 solar in all shells. This was assumed because for cool gas with approximately solar abundance of heavy elements, the contributions of continuum and lines are difficult to disentangle unambiguously, resulting in an anti-correlation between the emission measure and abundance.

Figure 1 shows generally a good agreement between the Chandra and XMM-Newton profiles in the region of overlap. NGC 1399, NGC 1407, NGC 4649 and NGC 5846 have deprojected temperature profiles that start around 1.0 keV in the central region, dip slightly towards 0.5 keV and then slowly increase outwards to about 1.5 keV. The temperature profile of NGC 4472 increases steadily from about 0.7 keV to 1.4 keV while the temperature profile of NGC 4486 increases much more steeply from about 1 keV to 3 keV with a small dip in between. The density profiles are much smoother than the temperature profiles. They appear to be very similar to

each other with a linear decrease in a log-log scale and are therefore close to power laws.

3 NON-PARAMETRIC RECONSTRUCTION OF THE MASS DISTRIBUTION

If the gas is in hydrostatic equilibrium, we can obtain the mass distribution from the deprojected gas temperature and density profiles. Here we describe a new non-parametric Bayesian approach to obtain the most probable mass profiles within some confidence range.

3.1 Hydrostatic equilibrium

Hydrostatic equilibrium relates the 3-D temperature and density profiles of the gas to the 3-D mass distribution of the galaxy. If the gas is relatively undisturbed, we can assume it is in hydrostatic equilibrium. Balancing the pressure of the gas with the gravitational forces acting on it in a spherical system gives:

$$-\frac{d\Phi(r)}{dr} = \frac{1}{\rho(r)} \frac{dP(r)}{dr} \quad (1)$$

where ρ is the gas mass density, P the gas pressure and r is the 3-D radius from the centre of the galaxy. We assume that the gas is ideal and therefore $P = nk_B T$ and $\rho = \mu m_p n$, where n is the particle number density of the gas, and $\mu = 0.61$ is the average gas particle mass in terms of the proton mass, m_p . This value of μ corresponds to a helium number density of 7.92×10^{-2} and 0.5 solar abundance of heavier elements. Now we have related the temperature and density of the gas to the gravitational potential it resides in. We can express Equation (1) in terms of the circular velocity curve, a distant-independent measure of the mass, $V_c^2 = rd\Phi/dr$. The circular velocity at some radius in a galaxy is the orbital velocity of a star at that radius on a circular orbit in the same gravitational field. Equation (1) becomes:

$$V_c^2 = -\frac{k_b T}{\mu m_p} \frac{d \ln P}{d \ln r} \quad (2)$$

It can be seen that to obtain the circular velocity curve, the temperature and gradient of the logarithmic pressure is required. This is more convenient than the usual form of this equation, where both the temperature and density derivatives are required.

3.2 Bayesian approach

We would like to find the most probable logarithmic pressure gradients (and then circular velocity curve from hydrostatic equilibrium) within some confidence range given the deprojected temperature and density profiles measured from the data. Merritt & Tremblay (1994) showed that it is best to treat these problems non-parametrically because parametric methods are susceptible to systematic biases and underestimate the confidence ranges. The procedure we develop can eventually incorporate the spectral fitting and deprojection directly, but in a first step we concentrate here on generalising parametric methods on deprojected profiles to

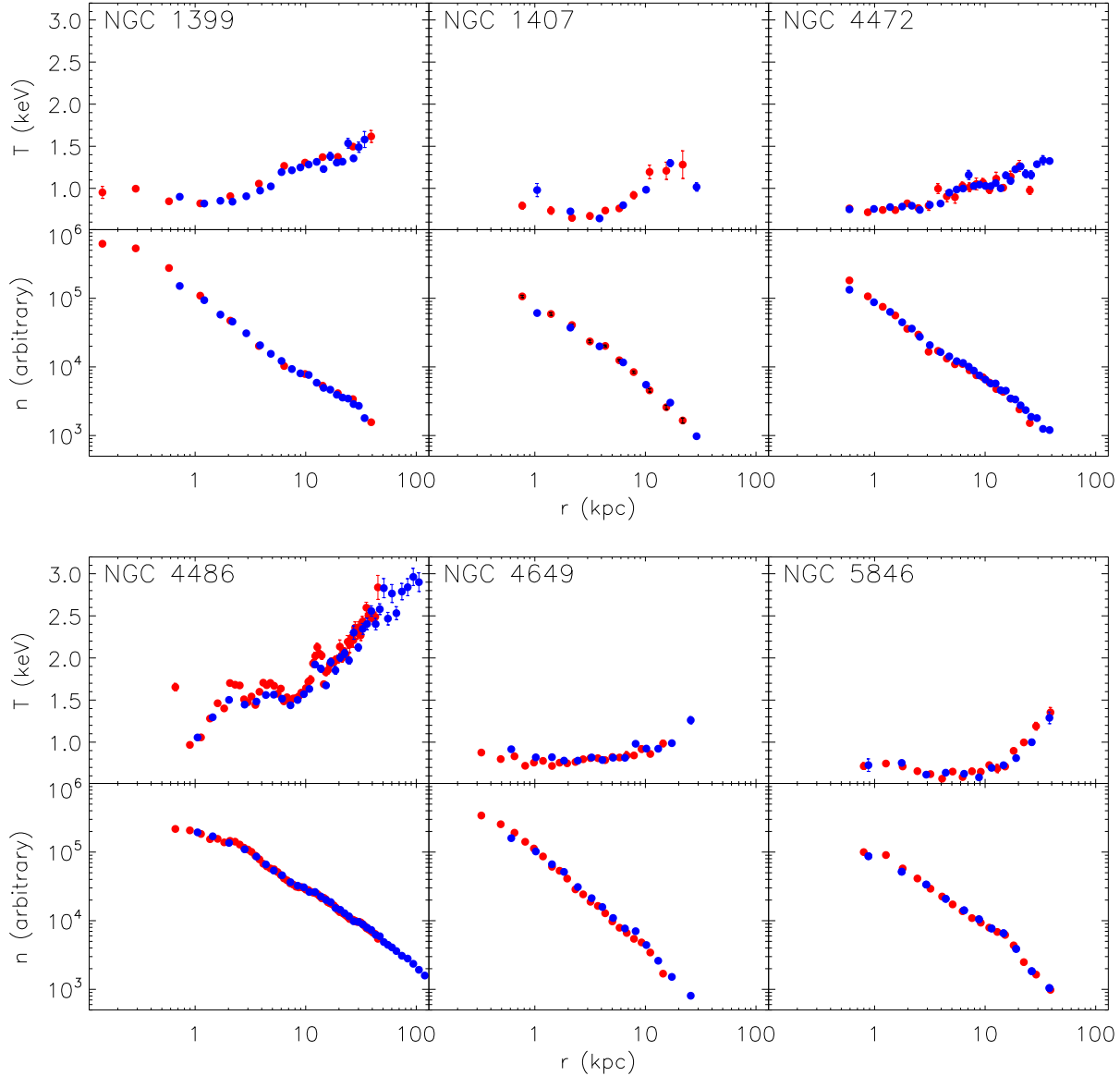


Figure 1. Properties of the hot gas surrounding the sample of six X-ray bright elliptical galaxies: Deprojected temperature (upper plot) and density profiles (lower plot) were obtained by Churazov et al. (2010) from the analysis of Chandra observations (red dots) and XMM-Newton observations (blue dots). The temperature is shown on a linear scale. The density and radii are shown on logarithmic scales.

non-parametric ones. We adopt a Bayesian approach rather than the more conventional method of χ^2 minimisation for two reasons: Firstly, prior information such as the intrinsic smoothness of the profiles is easily incorporated. Secondly, the probabilistic nature of Bayesian methods means confidence ranges are more easily extracted.

Let us describe the galaxy by some model M . Bayes' theorem tells us the probability of M given the deprojected

temperature and density profiles X from the X-ray observations:

$$p(M | X) = \frac{p(X | M)p(M)}{p(X)} \quad (3)$$

Taking the logarithm of both sides gives:

$$\ln(p(M | X)) = \ln(p(X | M)) + \ln(p(M)) - \ln(p(X)) \quad (4)$$

$p(M | X)$ is the posterior probability of the model given the deprojected temperature and density profiles. $p(X | M)$ is the likelihood probability $\mathcal{L}(M)$ of the deprojected temperature and density profiles given the model. $p(M)$ is the prior probability of the model, indicating what we thought about the probability of that model before we knew anything about the deprojected temperature and density profiles. Finally $p(X)$ is the probability of those particular deprojected density and temperature profiles, but here only acts as a normalising factor because the profiles are fixed by the X-ray observations. To obtain the most probable model profile, we need to maximise the posterior probability $p(M | X)$. In order to find all model profiles within some confidence range we have to find the shape of the posterior probability distribution.

We define our model $M = M(T, lpg, P, V_c, m)$, where T is the temperature, lpg is the logarithmic pressure gradient, P is the pressure, V_c is the circular velocity and m is the enclosed mass. The pressure P is obtained by integrating the logarithmic pressure gradient lpg . The circular velocity V_c is obtained by applying hydrostatic equilibrium, and the mass m follows from $V_c^2 = Gm/r$. The model T and P are compared with the deprojected T_{depro} and P_{depro} obtained from the X-ray observations and deprojection. The model functions are defined on a grid of n_{mod} logarithmically-spaced radii r , finer than the grid of n_{depro} deprojected radii r_{depro} . We interpolate the functions to the grid of deprojected radii for the calculation of the χ^2 function below. We shall use j to denote an element on the model grid and k to denote an element on the deprojected grid. For example, $T[j]$ denotes the model temperature at the radius $r[j]$ on the model grid and $T[k]$ denotes the model temperature at the radius $r_{\text{depro}}[k]$ on the deprojected grid.

We assume that the likelihood function $\mathcal{L}(M)$ takes the form of a multi-variate Gaussian:

$$\mathcal{L}(M) \propto \exp(-\chi^2/2) \quad (5)$$

χ^2 is the goodness-of-fit of the model temperature to the deprojected temperature and the model pressure to the deprojected pressure:

$$\chi^2 = \sum_{k=1}^{n_{\text{depro}}} \left(\frac{P_{\text{depro}}[k] - P[k]}{\epsilon_P[k]} \right)^2 + \sum_{k=1}^{n_{\text{depro}}} \left(\frac{T_{\text{depro}}[k] - T[k]}{\epsilon_T[k]} \right)^2 \quad (6)$$

where ϵ_P and ϵ_T are $1\text{-}\sigma$ statistical errors on the deprojected pressure and temperature profiles respectively. This choice for the likelihood function assumes a Gaussian error distribution and can be generalised if needed. To enforce physically acceptable solutions, we impose the following boundary conditions as priors on the model temperature and logarithmic pressure gradient profiles:

- (i) $T \geq 0$
- (ii) $V_c \in \mathfrak{R} \Rightarrow lpg \leq 0$

We also need to define a smoothing prior because unlike in a parameterised model, the best-fit non-parametric model would go exactly through all the deprojected temperature and density points resulting in noisy profiles. Also, as the model grid is finer than the deprojected grid, without smoothing there would be many solutions where the

model is very similar to the deprojected temperature and density at the deprojected radii but with varying values in between. Therefore applying smoothing constraints reduces the model degeneracies by getting rid of unphysical solutions. We specifically penalise non-smooth solutions of the model temperature, logarithmic pressure gradient and resulting circular velocity curve because this is consistent within the hydrostatic framework. We define the smoothing prior as follows:

$$p(M) \propto \exp(-S) \quad (7)$$

S is a weighted sum of the mean-square second derivatives of the temperature, logarithmic pressure gradient and circular velocity curve:

$$S = c(S_1 + S_2 + S_3) \quad (8)$$

$$S_1 = \sum_{j=2}^{n_{\text{mod}}-1} \left(\frac{\ln T[j+1] - 2 \ln T[j] + \ln T[j-1]}{h^2} \right)^2 \quad (9)$$

$$S_2 = \sum_{j=2}^{n_{\text{mod}}-1} \left(\frac{lpg[j+1] - 2lpg[j] + lpg[j-1]}{h^2} \right)^2 \quad (10)$$

$$S_3 = \sum_{j=2}^{n_{\text{mod}}-1} \left(\frac{\ln V_c[j+1] - 2 \ln V_c[j] + \ln V_c[j-1]}{h^2} \right)^2 \quad (11)$$

h is the logarithmic interval between the model radii in an equally-spaced logarithmic radial grid and $c = n_{\text{depro}}\lambda/(n_{\text{mod}} - 2)$ determines the weight of the smoothing term relative to the χ^2 term. It is defined so that for fixed λ , the smoothing term is independent of n_{depro} and n_{mod} . λ is specified by the user and Section 4.2 describes how we choose its optimal value. As the second derivatives are difficult to estimate at the boundaries, we omit their contribution to the smoothing prior.

Combining the likelihood function and the priors we get the following expression for the logarithm of the posterior probability, which we call F :

$$F = \ln(p(M | X)) = -\frac{\chi^2}{2} - S + N \quad (12)$$

N is a normalisation constant, which we set to zero for convenience.

3.3 The distribution of posterior probabilities

Now that we have defined our model and the posterior probability of a particular model given the X-ray information, we need an initial model and a procedure to generate new models in order to find the distribution of posterior probabilities. Here we will discuss our initial model and the ‘proposal function’, a function used to generate a new model. We then describe an algorithm we implement, optimised to find the most probable model. This is similar to the method of Magorrian (1999), who found the most probable 3-D distribution of stars given a projected surface-brightness distribution. We also describe a second algorithm based on the Metropolis-Hastings sampling scheme in a Markov Chain

Monte Carlo (MCMC) approach, optimised to extract confidence ranges associated with a model. We define an ‘iteration’ as a change proposed by the proposal function that lies within the boundary conditions.

3.3.1 The initial model

The initial model is given by $M_{\text{init}}(T_{\text{init}}, lpg_{\text{init}}, P_{\text{init}}, V_{c,\text{init}}, m_{\text{init}})$, calculated on the model grid. T_{init} is determined by fitting a highly smoothed spline to the deprojected temperature T_{depro} . lpg_{init} is set to the slope of a straight-line fit between the logarithm of the deprojected pressure, P_{depro} and the logarithm of the deprojected radii, r_{depro} . $V_{c,\text{init}}$ and m_{init} follow from applying hydrostatic equilibrium (Equation (2)), and the posterior probability of this initial model F_{init} can be calculated using Equation (12).

3.3.2 The proposal function

The proposal function $q(M_{i+1} | M_i)$ is a probability distribution that generates a model M_{i+1} from model M_i . We only make changes to the model T and lpg and then calculate the resulting model P from integrating lpg and the model V_c and m by applying hydrostatic equilibrium. The proposal function is defined as:

$$q(M_{i+1} | M_i) = p[j] G_T[j] G_{lpg}[j] \quad (13)$$

$p[j] = 1/n_{\text{mod}}$, is the probability of picking point j on the model grid. $G_T[j] = p(T_{i+1}[j] | T_i[j])$ is the probability of going from $T_i[j]$ to $T_{i+1}[j]$ and $G_{lpg}[j] = p(lpg_{i+1}[j] | lpg_i[j])$ is the probability of going from $lpg_i[j]$ to $lpg_{i+1}[j]$, at the chosen grid point j . $G_T[j]$ and $G_{lpg}[j]$ are described by Gaussians centred on $T_i[j]$ and $lpg_i[j]$ respectively and with dispersions $\sigma_T[j]$ and $\sigma_{lpg}[j]$. σ_T is initially set to the root-mean squared deviation between T_{init} and T_{depro} , and σ_{lpg} is initially set to the root-mean squared deviation between lpg_{init} and a two-point estimate of the logarithmic pressure gradient.

3.3.3 Obtaining the most probable solution (non-Markov mode)

To obtain the most probable model we want to get to the maximum of the posterior probability distribution as quickly as possible. We first relax the initial model to mitigate any bias introduced in choosing it. In this phase the proposal function is used to make a change to the model at a random point on the model grid. If the boundary conditions are met, then the proposed change is accepted and the new posterior probability F and change in posterior probability ΔF are calculated. After n_{relax} iterations, the relaxation phase ends and the average change in the posterior probability $\langle \Delta F \rangle$ is calculated. In the relaxation phase, it is possible for $\langle \Delta F \rangle$ to be either negative or positive as we accept all changes subject to the boundary conditions.

In the improvement phase, a change to the model is proposed via the proposal function and if the boundary conditions are met then an acceptance probability α is specified for going from model M_i to model M_{i+1} :

$$\alpha(i, i+1) = \min(1, r) \text{ where } r = \exp \frac{\Delta F}{\langle \Delta F \rangle} \quad (14)$$

A random number z is generated between 0 and 1. If $z \leq \alpha(i, i+1)$, the proposed change is accepted and the dispersion of the proposal function is decreased, $\sigma_T[j] = \sigma_T[j]/u$ and $\sigma_{lpg}[j] = \sigma_{lpg}[j]/u$, where $u = 1.01$ to allow for fine changes. Otherwise the proposed change is rejected and $\sigma_T[j] = \sigma_T[j] \times u$ and $\sigma_{lpg}[j] = \sigma_{lpg}[j] \times u$. This update to the proposal function is made after each change to the model so that in general we follow a path that maximises the posterior probability, but still allow for the possibility of jumping away from a local maximum. The value for $\langle \Delta F \rangle$ is updated every n_{log} steps.

This procedure is continued until the model no longer significantly changes.

3.3.4 Obtaining the confidence range (Markov mode)

To obtain the confidence range we need to probe the shape of the posterior probability distribution. The most efficient way to do this is using the Metropolis-Hastings algorithm, which generates models with a probability equal to the posterior probability. In our implementation of this algorithm we have three phases. The first is a relaxation phase of the initial model as in Section 3.3.3 with n_{relax} iterations. The second is a tuning of the proposal function, where the proposal function is updated as in the second phase in Section 3.3.3. This phase ends after n_{tune} steps, defined such that the acceptance rate in the third phase is 23%. This is recommended as the most efficient rate for probing the shape of the posterior probability distributions in high-dimensional implementations of the Metropolis-Hastings algorithm (Liddle 2009).

In the third phase we want to map out the shape of the posterior probability distribution around the maximum. The proposed changes must therefore satisfy ‘detailed balance’:

$$p(M_i | X) p(M_{i+1} | M_i) = p(M_{i+1} | X) p(M_i | M_{i+1}) \quad (15)$$

$p(M_{i+1} | M_i) = q(M_{i+1} | M_i) \alpha(i, i+1)$ and $p(M_i | M_{i+1}) = q(M_i | M_{i+1}) \alpha(i+1, i)$, where the proposal function q and acceptance probability α were defined in Equations (13) and (14) respectively. This is ensured by no longer changing the proposal function and replacing the definition of r from Equation (14) with:

$$r = \exp \Delta F \quad (16)$$

r is called the Metropolis ratio. This will produce a sequence of models called a Markov chain. This is continued until the Markov chain converges to the posterior probability distribution. The initial ~ 25 – 50% of the accepted changes is called the ‘burn-in phase’ and is discarded because they do not reflect the posterior probability distribution. The convergence of the Markov chain can be checked by looking at the distribution of model values at each grid point and ensuring that subsequent iterations produce insignificant changes.

Marginalisation with a Markov chain is trivial because the density of any grid point in the Markov chain will be proportional to the posterior distribution marginalised over

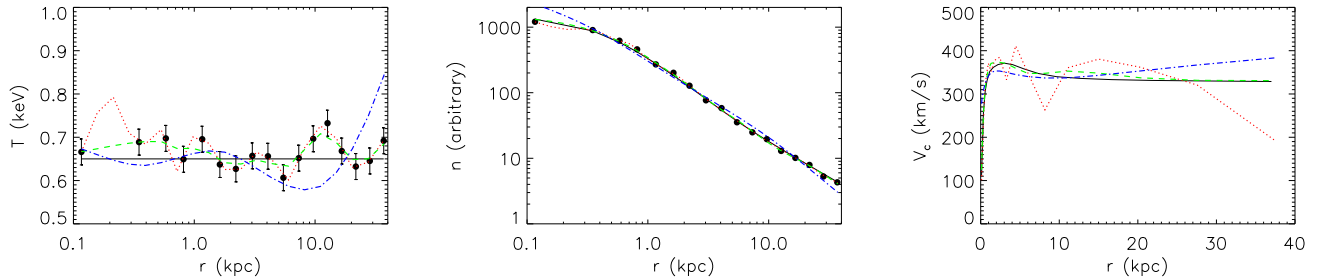


Figure 2. Application of the non-parametric analysis to a test model: The black lines show the (i) temperature, (ii) density and (iii) circular velocity curves for our test model. The filled black circles show the pseudo temperature and density profiles. The remaining lines show recovered profiles from pseudo deprojected temperature and density profiles generated from the test model, assuming $\lambda = 0.001$ (red, dotted), $\lambda = 0.5$ (green, dashed) and $\lambda = 100$ (blue, dash-dotted).

the other variables. The shape of the marginal posterior density at each grid point will tell us the median and confidence ranges, and the expectation value is simply a mean of all the values generated in the Markov chain.

4 TESTS

We need to test the ability of the two methods to recover the circular velocity curve of a galaxy and to choose values for the parameters n_{relax} , n_{log} , n_{burnin} , n_{iter} and λ that we have introduced in Section 3.2, 3.3.3 and 3.3.4.

For the relaxation phase we set $n_{\text{relax}} = 3(2n_{\text{mod}})$, similar to that used by Magorrian (1999). In the non-Markov mode we set $n_{\text{log}} = 8(2n_{\text{mod}})$, again similar to that used by Magorrian (1999). In the Markov mode we set n_{burnin} to 25% of the total number of accepted changes to ensure we are only sampling the posterior probability distribution. We choose the total number of accepted changes n_{iter} as the number of iterations after which the model no longer appears to change significantly.

To test the two modes of operation and calibrate the number of accepted changes n_{iter} and the smoothing parameter λ , we define a model of a typical X-ray bright elliptical galaxy, from which we draw pseudo 3-D temperature and density profiles.

4.1 The test model and pseudo temperature and density profiles

The test model is defined by a 3-D temperature profile, 3-D density profile and a circular velocity curve $[T_{\text{test}}, n_{\text{test}}, V_{c,\text{test}}]$ typical for a X-ray bright elliptical galaxy. These profiles are shown by the black lines in Figure 2. For the circular velocity curve we use the dynamical model of NGC 5846 by Kronawitter et al. (2000). We assume the temperature T_{test} is constant at 0.65 keV and then calculate the corresponding lpg_{test} and density (n_{test}) profiles. n_{test}^2 is projected and pure Poissonian statistics typical for XMM-Newton is added. The projected density profiles are then deprojected as in Churazov et al. (2008) and a deprojected density profile is obtained. We added Gaussian random deviates to the temperature assuming a constant error of 0.03 keV to complete the set of pseudo deprojected profiles shown with filled black circles in Figure 2.

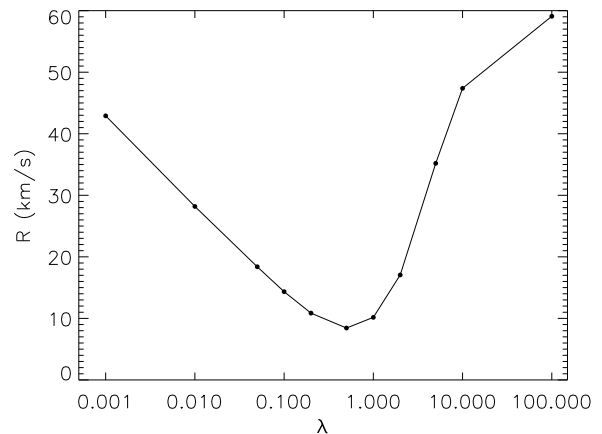


Figure 3. Residuals between the circular velocity curve of the test model and the circular velocity curves recovered by the non-parametric analysis for different values of the smoothing parameter, λ .

4.2 Choice of optimal smoothing parameter

We use our method in the non-Markov mode to obtain the best-fit circular velocity curve for different values of λ from the pseudo deprojected temperature and density profiles. We find that $n_{\text{iter}} = 10^6$ iterations is sufficient to reach a best-fit model.

A plot of the root-mean squared deviation R between the recovered circular velocity curve of the test model and the input circular velocity curve, against the smoothing parameter λ , is shown in Figure 3 where:

$$R = \left[\frac{\sum (V_{c,\text{test}} - V_{c,\text{mod}})^2}{n_{\text{mod}}} \right]^{1/2} \quad (17)$$

Figure 3 shows that R has a minimum at around $\lambda_{\text{opt}} = 0.5$. A lower smoothing leads to unphysical fluctuations in the recovered model and a higher smoothing results in a recovered model that does not fit the temperature and density profiles of the test model well.

Figure 2 shows the resulting best-fit temperature, den-

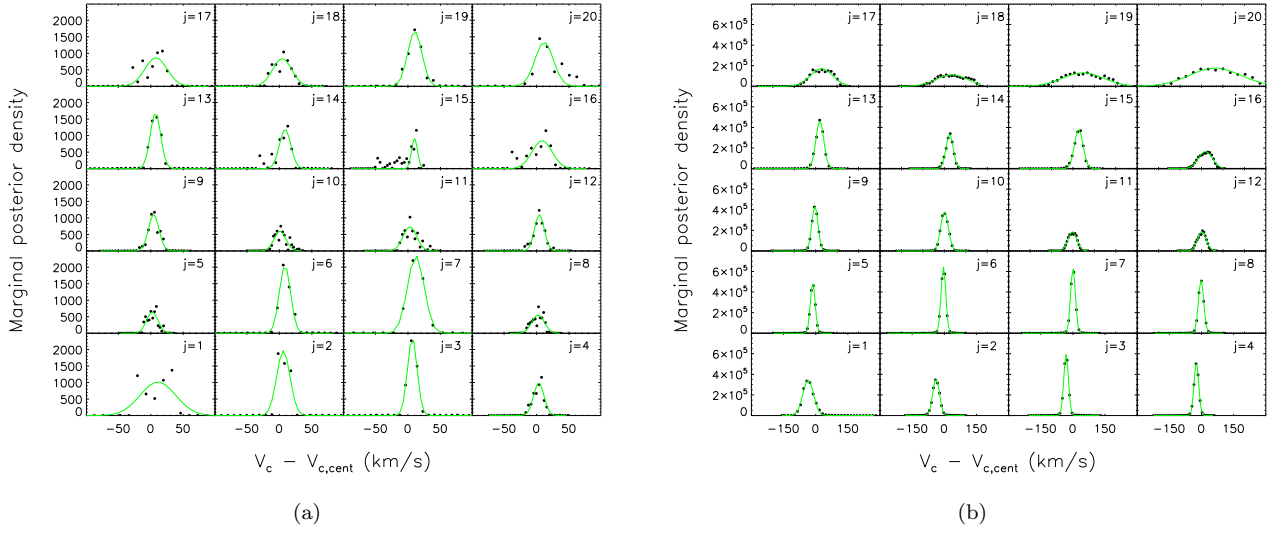


Figure 4. The circular velocity values V_c generated at each grid point j from our non-parametric analysis of the pseudo deprojected temperature and density profiles: The filled black circles show the binned number density (proportional to the marginal posterior density) of V_c values at each grid point j for (a) $n_{\text{iter}} = 10^4$ and (b) $n_{\text{iter}} = 2 \times 10^6$ and the green lines show the best-fit Gaussians.

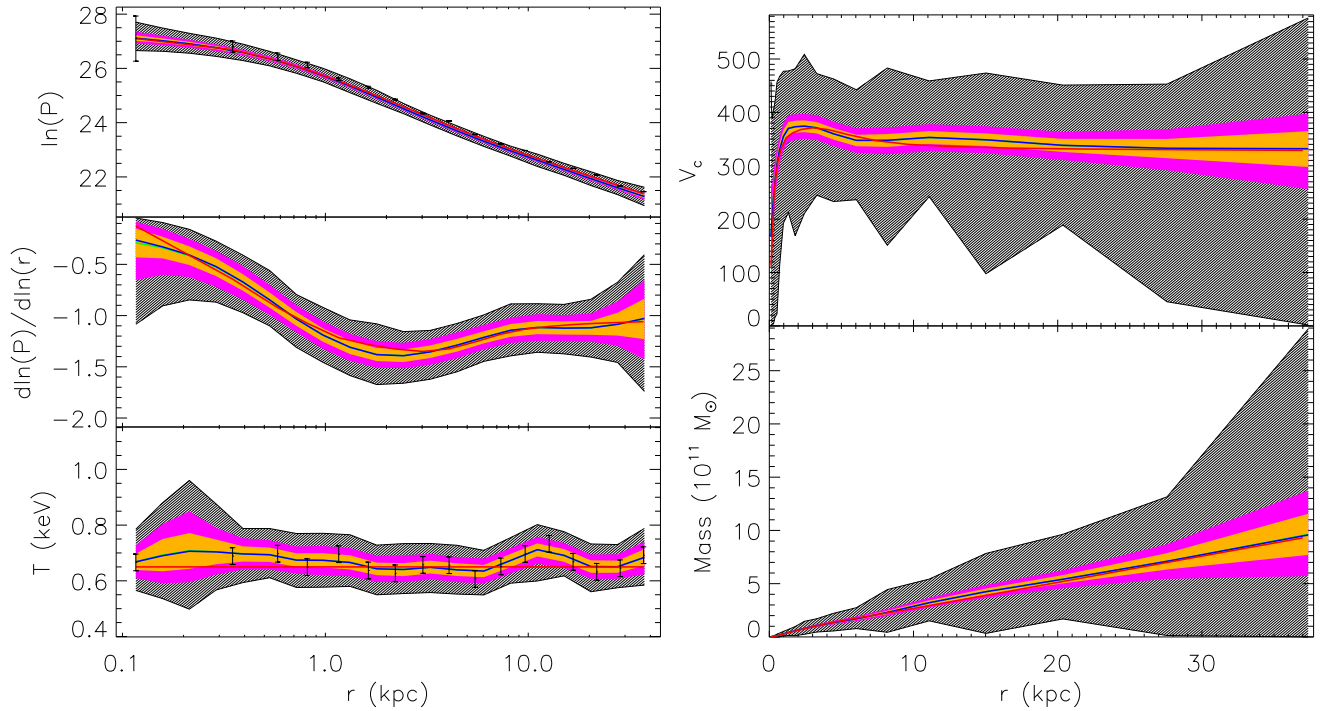


Figure 5. Application of the non-parametric analysis to the pseudo deprojected temperature and density profiles: Going counter-clockwise from the top left are the (i) logarithmic pressure, (ii) logarithmic pressure gradient, (iii) temperature, (iv) mass and (v) circular velocity profiles. The left three profiles are on a logarithmic radial scale, while the two profiles on the right are on a linear radial scale. The red lines correspond to the input test model, the green lines correspond to the recovered expected profiles and the blue lines correspond to the recovered median profiles. The grey region shows all generated points, the pink region shows the 95% confidence range and the orange region shows the 68% confidence range.

Galaxy (1)	χ^2_T (2)	χ^2_{lnP} (3)	M_{25} ($10^{11} M_\odot$) (4)	$V_{c,25}$ (km/s) (5)	ζ (6)	$\zeta_{<10}$ (7)	$\zeta_{>10}$ (8)
NGC 1399	2.7	10.1	13.2 ± 1.1	475.0 ± 20.9	1.15 ± 0.03	1.16 ± 0.06	1.60 ± 0.06
NGC 1407	1.4	3.8	21.6 ± 7.0	608.9 ± 97.9	1.26 ± 0.07	0.88 ± 0.05	1.26 ± 0.09
NGC 4472	2.7	4.9	14.1 ± 1.0	491.8 ± 17.0	1.19 ± 0.02	1.02 ± 0.02	1.59 ± 0.01
NGC 4486	16.2	28.9	15.7 ± 0.6	520.3 ± 9.3	1.36 ± 0.01	1.60 ± 0.04	1.37 ± 0.01
NGC 4649	3.0	9.4	16.4 ± 4.3	530.4 ± 69.7	1.13 ± 0.01	1.08 ± 0.01	1.38 ± 0.01
NGC 5846	2.3	3.7	12.5 ± 1.9	463.2 ± 35.0	1.17 ± 0.05	0.88 ± 0.05	2.16 ± 0.02

Table 2. Derived properties of the sample of six X-ray bright elliptical galaxies: (1) Galaxy name, (2) χ^2 per data point between deprojected temperature and model temperature, (3) χ^2 per data point between deprojected logarithmic pressure and model logarithmic pressure, (4) enclosed mass at 25 kpc and associated 95% confidence range, (5) circular velocity at 25 kpc and associated 95% confidence range, (6) power-law index of mass profiles on a log-log scale and associated 1- σ error, (7) power-law index of mass profiles on a log-log scale fitting only until 10 kpc and associated 1- σ error and (8) power-law index of mass profiles on a log-log scale fitting only above 10 kpc and associated 1- σ error.

sity and circular velocity curves for the minimum (0.001), maximum (100) and optimal (0.5) values for λ .

4.3 Confidence range on recovered circular velocity curve

To obtain the range of circular velocity curves within some confidence level, we have to ensure that our method is correctly probing the shape of the posterior probability. Assuming the optimal smoothing parameter found above, we now use the Markov mode on the pseudo profiles. $n_{\text{tune}} = 2000$ results in an acceptance rate of about 23% in the subsequent proposed changes. We use a higher $n_{\text{iter}} = 2 \times 10^6$, above which the profiles change insignificantly and choose $n_{\text{burnin}} = 5 \times 10^5$, above which the expectation values calculated change insignificantly. In Figure 4 we have plotted how the circular velocity points at each radius are distributed in the Markov chain (i.e. after the burn-in phase), to illustrate the difference between using a n_{iter} that is too low and one that is about right. In the left plot where $n_{\text{iter}} = 10^4$ and $n_{\text{burnin}} = 5000$, the distribution of circular velocity points at each radius (i.e. the marginal posterior probability of the circular velocity curve at each grid point) have not settled to a smooth distribution, and therefore one would suspect that the chain is not yet properly sampling the posterior probability distribution. The plot on the right however shows that running the Markov chain for longer results in smooth marginal posterior probability distributions that are well described by Gaussians (illustrated by the green lines).

From Figure 4(b) the median value for the circular velocity at each radius is the circular velocity for which the marginal posterior probability is highest. The expectation value is the mean of all the circular velocity values chosen at that radius and the associated $c\%$ confidence range is given by the extrema of $c\%$ of the circular velocity values with the highest marginal posterior probabilities. Figure 5 shows the results of calculating these for all the model profiles. One can see that the median and expected profiles lie on top of each other, showing that the marginal posterior probability distributions at each radius are symmetrical. It can also be seen that the test model profiles lie within or on the boundary of the 68% confidence range. We repeat this for different sets of pseudo deprojected density and temperature profiles and we are convinced that the procedure is able to recover the circular velocity curve without a systematic bias.

5 TOTAL, STELLAR AND DARK MATTER MASS PROFILES

Now that we have tested the method, we can apply it to the sample of six X-ray bright elliptical galaxies to derive total mass and circular velocity profiles (Figure 6 and Table 2). We then estimate the stellar contribution to the total mass profiles using optical photometric data and stellar population models. Assuming negligible gas mass, we subtract the stellar mass from the total mass profiles to infer the dark matter mass fractions.

5.1 Total mass profiles and circular velocity curves

The fits to the deprojected logarithmic pressure and temperature profiles and the derived logarithmic pressure gradient, circular velocity and mass profiles are shown in Figure 6, for the sample of six galaxies. Columns (2)–(7) in Table 2 list the χ^2 per data point of the expected models, the enclosed mass and associated 95% confidence range at 25 kpc and the circular velocity and associated 95% confidence range at 25 kpc. We choose 25 kpc because the deprojected profiles for all the galaxies extend at least as far as this radius. We quote the χ^2 per data point rather than the χ^2 per degrees of freedom because the latter is unknown. The degrees of freedom is equal to the number of constraints subtracted by the number of parameters. In our case the number of constraints is the number of data points plus the number of constraints introduced by the smoothing, which is difficult to define.

Generally, the fits in the mean are very good. The χ^2 per data point between the deprojected temperature and model temperature ranges from 1.4 to 16.2. The χ^2 per data point between the deprojected logarithmic pressure and model logarithmic pressure ranges from 3.7 and 28.9. The χ^2 values are not comparable to the usual reduced χ^2 which is ~ 1 at the 1- σ level, because the reduced χ^2 is normalised by the number of degrees of freedom. Our χ^2 values may also be higher than expected because we have only considered statistical errors on the deprojected temperature and pressure profiles. There is also correlated/anti-correlated scatter in the deprojected temperature profiles between adjacent points as a result of the deprojection procedure (Churazov et al. 2008). AGN activity driving shock

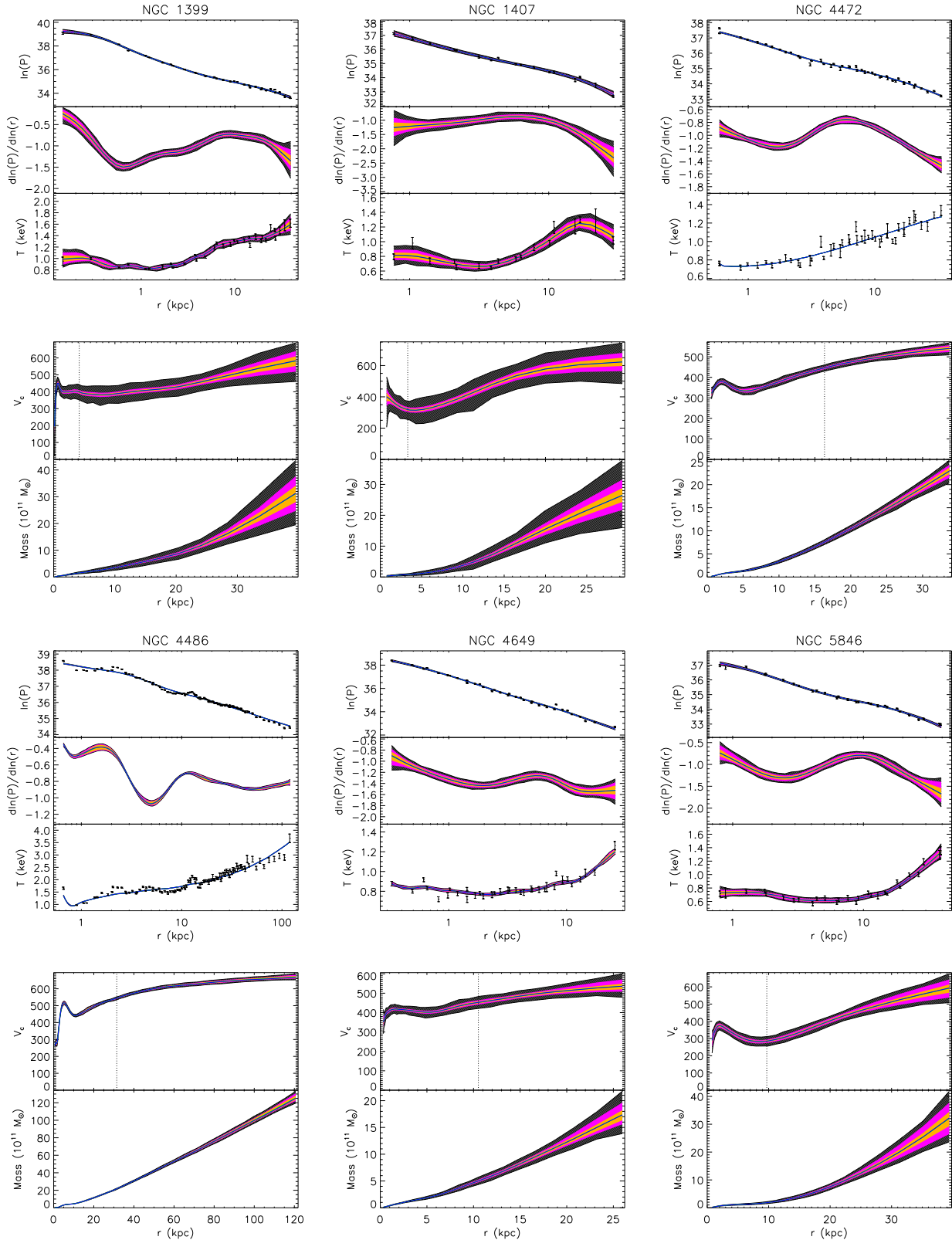


Figure 6. Application of the non-parametric analysis to the sample of six X-ray bright elliptical galaxies: Going from top down for each galaxy are shown the (i) logarithmic pressure, (ii) logarithmic pressure gradient, (iii) temperature, (iv) circular velocity and (v) mass profiles. The top three profiles are on a logarithmic radial scale, while the bottom two are on a linear radial scale. Black points on the logarithmic pressure and temperature plots show the deprojected profiles and associated statistical errors. The green and blue profiles (often indistinguishable) correspond to the expected and median profiles respectively. The grey region shows all generated points, the pink region shows the 95% confidence range and the orange region shows the 68% confidence range. The vertical black dotted lines on the circular velocity plots are at $1R_e$, given in Table 3.

Galaxy (1)	Source (2)	Band (3)	Seeing (") (4)	R_e (kpc) (5)	Source (6)	R_2 (", kpc) (7)	$M/L(M_\odot/L_\odot)$ (8)	Source (9)
NGC 1399	S00	<i>B</i>	0.05	4.17	K10	2.9, 0.28	9.7	Kr00
NGC 1407	Sp08	<i>B</i>	1	3.32	H09	2.7, 0.38	4.2	Z07
NGC 4472	K09	<i>V</i>	0.05	16.34	H09	3.5, 0.28	6.0	T00
NGC 4486	K09	<i>V</i>	0.05	31.44	H09	7.6, 0.59	7.0	G09
NGC 4649	K09	<i>V</i>	0.05	10.52	H09	4.2, 0.34	7.8	T00
NGC 5846	Kr00	<i>V</i>	0.2	9.70	Kr00	3.3, 0.39	7.2	T00

Table 3. Photometric data for the sample of six X-ray bright elliptical galaxies: (1) Galaxy name, (2) source of surface-brightness profiles, (3) band of photometry, (4) seeing values, (5) effective radii, (6) source of effective radii, (7) radius at which the optical surface-brightness profile has a gradient of 2, (8) stellar population mass-to-light ratios converted to the photometric band in column (3) and distances from Table 1, and (9) source of stellar population mass-to-light ratios. References are S00 (Saglia et al. 2000), Sp08 (Spolaor et al. 2008), K09 (Kormendy et al. 2009), Kr00 (Kronawitter et al. 2000), K10 (J. Kormendy, *private communication*), H09 (Hopkins et al. 2009), Z07 (Zhang et al. 2007), T00 (Trager et al. 2000), G09 (Gebhardt & Thomas 2009).

waves into the ICM (e.g. Forman et al. 2007) can also result in systematic undulations in the measured temperature and density profiles. The models do not fit the deviations caused by the correlated/anti-correlated errors and by systematic errors because we have calibrated the smoothing to a test model of an ideal massive elliptical galaxy. If the statistics of the data are low as in the case of NGC 1407, then the error bars cover the correlated/anti-correlated scatter and the χ^2 values are low. The outstanding statistics (~ 0.5 Ms of Chandra observation) and very high surface brightness of NGC 4486 enables deprojected temperature and density profiles to be obtained in much narrower bins than for the other galaxies. This allows systematic deviations to be resolved, but as the errors bars are small, they do not cover the correlated/anti-correlated scatter or the systematic deviations. As a result the χ^2 values for NGC 4486 are on average about 5 times higher than for the other galaxies.

The general shape of the derived circular velocity curves can be summarised by a steep rise in the centre (except in NGC 1407) followed by a slight dip at a few to 10 kpc and then a more gentle rise outwards, reaching circular velocities of 463–609 km/s at 25 kpc. The outward rise in the circular velocity curves is a combined result of temperature profiles that rise outwards *and* logarithmic pressure gradients that increase in magnitude outwards. The dips in the circular velocity curves are a result of dips in the logarithmic pressure gradient around the same radius. These dips may reflect true changes in the mass distribution or they may be a result of shocks in the gas propagating outwards. Shock waves can be produced by an unsteady outflow of relativistic plasma from a central black hole, as in NGC 4486 (Churazov et al. 2008). The shockfront is characterised by a sharp increase in the pressure inwards and then a decrease in the rarefaction region behind the shock. This manifests itself as a dip in the circular velocity curve at the position of the shockfront in NGC 4486.

The enclosed mass profiles of all galaxies increase outwards with an increasing gradient as expected from the increasing circular velocity curves, pointing towards non-isothermal mass profiles. The 95% confidence ranges in the circular velocities and enclosed masses at 25 kpc are reasonably small and are smallest for the galaxies with the best statistics (NGC 4472 and NGC 4486) because the χ^2 values are higher as discussed above.

5.2 The stellar mass contribution

To estimate the stellar contribution to the total circular velocity curve, we use surface-brightness profiles from various sources in the literature, given in column (2) in Table 3 and shown in Figure 7(a). We deproject the surface-brightness profiles assuming a spherical stellar distribution and a power law outside the range of the data. We then integrate the resulting 3-D luminosity density profile to obtain the luminosity profile of the stars. Assuming constant stellar mass-to-light ratios with radius (columns (8) and (9) in Table 3), we obtain stellar mass profiles and stellar circular velocity curves from the luminosity profiles.

In order to find a scaling radius that best represents the luminosity of the stellar component, we examine two alternatives. The first is the mean effective radius, given in Table 3 for the sample of six galaxies. For NGC 1399 we use the determination of J. Kormendy (*private communication*) based on photometry in Caon et al. (1994) and Lauer et al. (2007). We calculate the mean effective radii from the major-axis effective radii and ellipticities for NGC 1407, NGC 4472, NGC 4486 and NGC 4649 determined by Hopkins et al. (2009) from photometry in Lauer et al. (2007) (NGC 1399), Bender et al. (1988) (NGC 1407) and Kormendy et al. (2009) (NGC 4472, NGC 4486 and NGC 4649). Hopkins et al. (2009) determined double-Sèrsic fits to the profiles but calculated the effective radii for the total profiles. We do not use their determination for NGC 1399 because it is based on photometry from Lauer et al. (2007), which only probes the central region. For NGC 5846, we use the mean de Vaucouleur’s effective radius from Faber et al. (1989). The effective radii of massive elliptical galaxies are large and therefore require extended surface-brightness profiles with excellent sky subtraction, which we believe is true in the case of the photometry of Kormendy et al. (2009), but not in the older photometry where the sky subtraction may not be so accurate. Therefore as an alternative, we also calculate R_2 (column (6) in Table 3), the radius at which $d\mu/d\log R = 2$, where μ is in magnitudes/arcsec². Figure 7(a) illustrates the similarity between the general shapes of the surface-brightness profiles when the radius is scaled by R_2 , and the surface brightness by its value at R_2 . We obtain values of R_2 ranging between 2.7–7.6", corresponding to 0.3–0.6 kpc, just outside typical seeing values of 1–2". Figure 7(a) shows that R_2 is located around the radius that

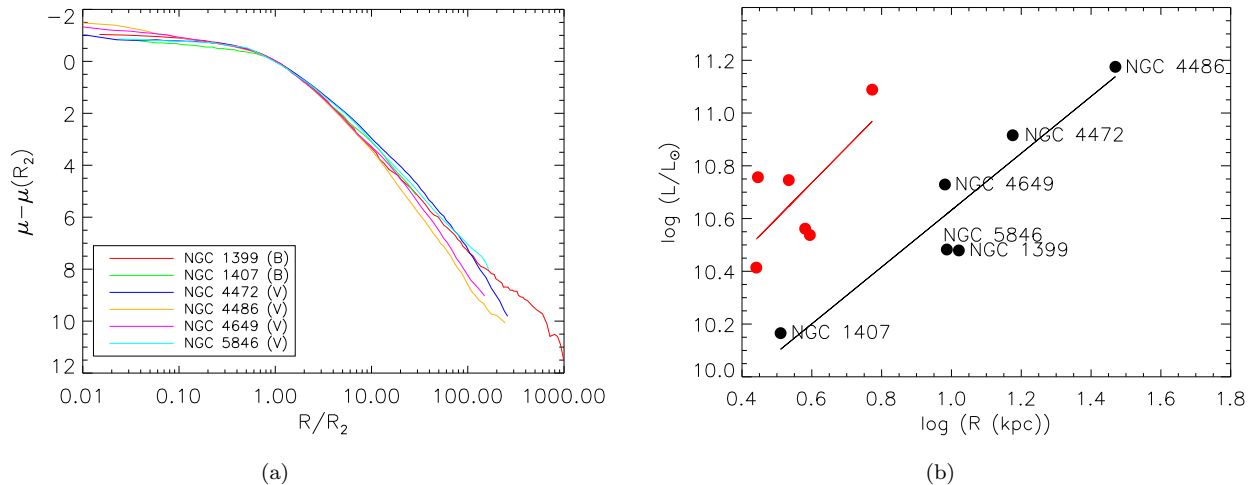


Figure 7. Luminous properties of the six X-ray bright elliptical galaxies: (a) Surface-brightness profiles scaled by R_2 (the radius where $d\mu/d\log R = 2$) and by the surface brightness $\mu(R_2)$. (b) Kormendy relation between the B -band luminosity $L_B(30R_2)$ and R_2 (red filled circles) and between the B -band luminosity $L_B(R_e)$ and R_e (black filled circles). $\log(R_2)$ has been shifted by 1 to the right. The straight red and black lines show the respective best-fit straight lines.

separates the core where the surface brightness decays gently, from the region where it starts decaying more steeply, and therefore may be mostly reflecting the core properties.

To determine which scaling radius should be used as representative of the galaxy’s luminosity, we plot an analogy to the Kormendy relation (Kormendy 1977) in Figure 7(b). We plot the B -band luminosity of the sample galaxies at $30R_2$ against R_2 and the B -band luminosity at $1R_e$ against R_e and fit straight lines through both. The best-fit straight lines have slopes of 0.74 and 0.93 and Pearson product moment correlation coefficient (PMCC) values of 0.70 and 0.94 respectively, supporting correlations at about 88% and 99% levels of significance for a sample size of six. The correlation between the effective radius and the luminosity of the stellar component is much stronger, and therefore we will use this to represent the size of the stellar component.

5.3 Scaled total circular velocity curves and dark matter mass fractions

Figure 8(a) shows the scaled total circular velocity profiles of the sample of X-ray bright galaxies from the X-rays along with the 95% confidence ranges with dashed lines. The radii are scaled by R_e and the total circular velocities are scaled by their value at R_e . In the central R_e , all the profiles rise steeply then fall again before rising more gently from $0.5-1R_e$. The outer rise in the circular velocity curves noted in Section 5.1, is more easily compared between the galaxies in this scaled plot. The curve of NGC 5846 rises most steeply. The curves of NGC 1399, NGC 1407, NGC 4472, NGC 4486 and NGC 4649 have a similar rise between $1-2R_e$ but the curves of NGC 1399 and NGC 1407 keep rising outwards, while the curve of NGC 4486 levels off outside $2R_e$.

The mass in gas calculated from integrating the gas density profiles is $< 0.04\%$ of the mass in stars in all galaxies except in NGC 4486 where it is $\sim 0.4\%$. Therefore we treat the gas mass as negligible and assume that the baryonic mass component in the galaxy is solely due to stars. Sub-

tracting the stellar mass determined in Section 5.2 from the total mass obtained from the X-rays gives the dark matter mass, shown as a fraction of the total mass in Figure 8(b), outside $0.6R_e$. Below this radius the dark matter fractions we obtain for some of the galaxies are below zero, which could be a result of either an overestimate in the stellar mass-to-ratios or an underestimate in the total circular velocity curves derived from the X-rays, the latter of which we discuss in more detail in Section 6.2. The dark matter fractions range between 50–80% at $2R_e \sim 6.5-59$ kpc in all galaxies except NGC 1407 where it is $\sim 35\%$. Even further out, the profiles appear to converge to a value between 80–90%, pointing uniformly to a massive dark matter halo. The larger range in the dark matter mass fractions further in is indicative of dark matter mass profiles that have different shapes. For example the dark matter mass profile is steepest for NGC 4486, implying a more compact dark matter component.

6 DISCUSSION

In this section we compare the circular velocity curves we obtain from our analysis to those obtained from previous X-ray determinations and published dynamical models. We then address the issue of the isothermality of the circular velocity curves and how this compares with the literature. Finally we look at how the total circular velocity curves may be correlated with properties of the stellar components and the velocity dispersions of the environments to which the galaxies belong.

6.1 Comparison with previous X-ray determinations

Figure 9 shows the total circular velocity curves for our sample of galaxies along with their 95% confidence ranges in black solid and dashed lines. For comparison we have

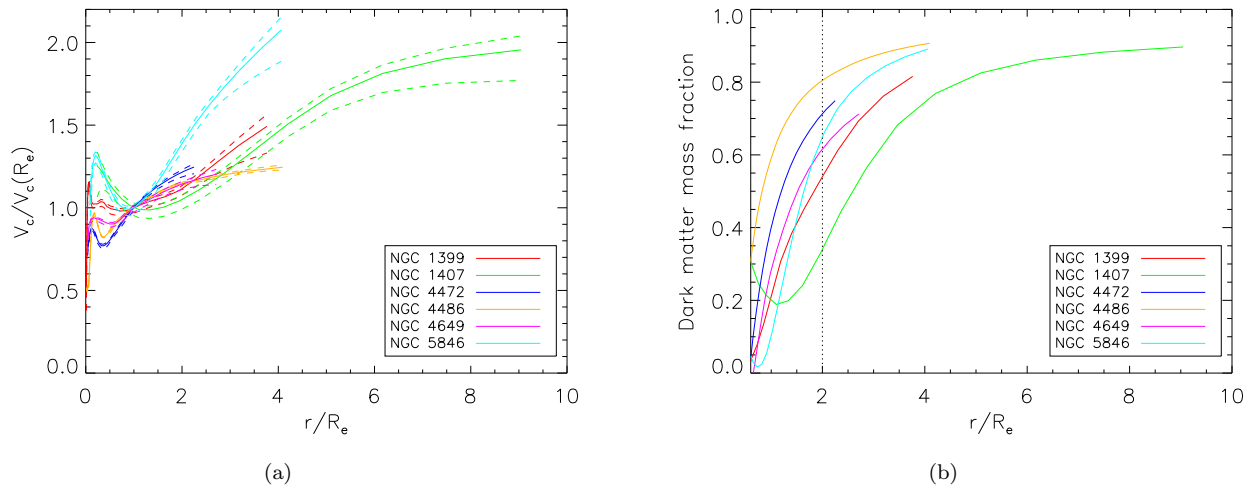


Figure 8. Total and dark matter mass properties of the six X-ray bright elliptical galaxies: (a) Total circular velocity profiles scaled by R_e in radius and the total circular velocity $V_c(R_e)$. (b) Dark matter mass fractions scaled by R_e in radius. The black dotted line highlights the dark matter mass fractions at $2R_e$.

overplotted various X-ray determinations in the literature. The green lines are from Fukazawa et al. (2006), who used Chandra observations of NGC 1399 and NGC 4472. The blue lines are from Nagino & Matsushita (2009) who combined Chandra and XMM-Newton observations of NGC 1399, NGC 4472 and NGC 5846, and the pink line is from Zhang et al. (2007) who combined Chandra and ROSAT data in NGC 1407. Humphrey et al. (2006) (solid orange lines), Humphrey et al. (2008) (dashed orange line) and Humphrey et al. (2009) (dotted orange line) used Chandra observations of NGC 1407, NGC 4472 and NGC 4649 and finally, the cyan line is from Matsushita et al. (2002), who used XMM-Newton observations of NGC 4486. Density and temperature profiles of the hot gas were obtained from the observations and parametrised. The total circular velocity curves were then obtained by differentiating the profiles and applying hydrostatic equilibrium.

Discrepancies in the outer slopes are most likely a result of differences in the spatial extent of the data used, as the last few points anchor the outer slope. Smaller-scale differences are most likely to arise from differences in the methods used to obtain the mass profiles. The methods employed in the literature are all parametric and therefore the shapes of the mass profile will have a systematic bias. In NGC 1407 however, the discrepancy between the outer slope of the circular velocity curve of Humphrey et al. (2006) and that of our determination and the determination of Zhang et al. (2007) is more significant than between the other profiles. The source of this is unclear.

6.2 Comparison with dynamical models

Figure 9 also shows dynamical models and their confidence ranges from the literature, in red solid and dashed lines. The vertical red dotted line demarcates the radial extent of the data used in the dynamical modelling and we plot the dynamical models to twice this radius, except in the case of NGC 1407 where we plot the models until the radius deemed

as reliable by the author. For NGC 1399 and NGC 5846, we use the spherical dynamical models of Kronawitter et al. (2000). They built models by superposing spherical distribution functions and adjusting the weights of their contribution to the model by comparing the projection of the model to measured surface-brightness profiles and long-slit kinematics extending to $97''$ and $99''$ respectively. Although this corresponds to only 5–10 kpc, the models provide a useful comparison in the central regions. 95% confidence ranges are provided on the models. For NGC 1407, we compare with the dynamical model of Romanowsky et al. (2009), who solved spherical Jeans equations for a varying anisotropy profile and fit to a surface-brightness profile and globular cluster kinematics extending out to $\sim 590''$. They provide a 68% confidence range on their model. For NGC 4472, NGC 4486 and NGC 4649 we compare with the models of Shen & Gebhardt et al. (2010, *in preparation*), Gebhardt et al. (2010, *in preparation*) and Shen & Gebhardt (2010), who used axisymmetric Schwarzschild models to fit surface-brightness profiles, integrated kinematics and globular cluster data extending to $1200''$, $500''$ and $533''$ respectively. 68% confidence ranges are provided on the models.

Comparing the X-ray circular velocity curves of this paper to those from dynamical models, we find that outside the central kpc in NGC 1399, the X-ray circular velocity curve is up to 16% lower than the dynamical modelling circular velocity curve. Outside a radius of about 7 kpc though, the X-ray determination lies within the 95% confidence range on the dynamical modelling determination. In the region of overlap between the X-ray and dynamical circular velocity curves of NGC 1407, the X-ray circular velocity curve rises from about 500 to 600 km/s, while the dynamical circular velocity curve rises from about 270 to 320 km/s, showing that the X-ray velocity curve is almost twice as high throughout and therefore rises twice as steeply. The X-ray circular velocity curve of NGC 4472 is up to 27% lower than the dynamical modelling circular velocity curve within about 12 kpc, but then rises to up to 20% higher outside this radius. Within 5 kpc, the X-ray circular velocity curve of NGC 4486 is up to

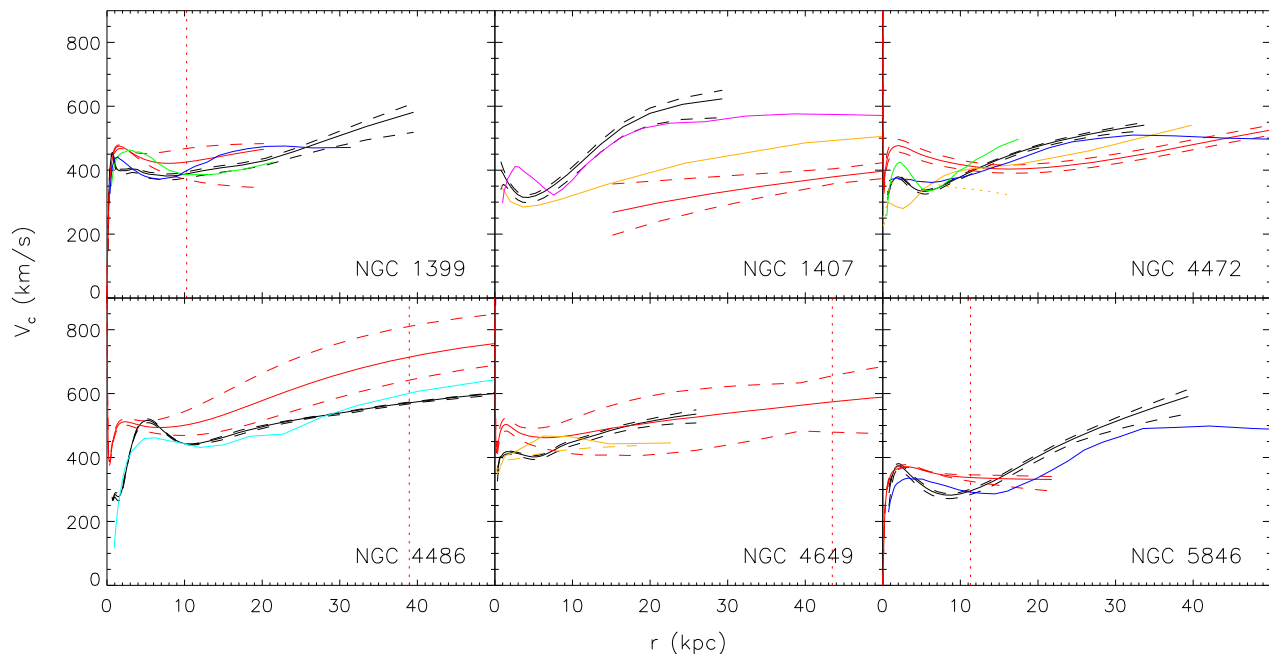


Figure 9. Total circular velocity curves determined from X-rays, compared with those from previous X-ray determinations and published dynamical models: The X-ray velocity curves and associated 95% confidence ranges determined in this paper are shown by the solid and dashed black lines respectively. Green lines (Fukazawa et al. 2006), blue lines (Nagino & Matsushita 2009), the pink line (Zhang et al. 2007), orange solid, dashed and dotted lines (Humphrey et al. 2006, 2008, 2009), and the cyan line (Matsushita et al. 2002) show circular velocity curves determined from X-rays in the literature. The best-fit dynamical models along with their confidence range (for more details see text) are shown with solid and dashed red lines. The vertical red dotted line shows the radial extent of the data used in the dynamical modelling.

45% lower than the dynamical circular velocity curve, and outside this region, the X-ray circular velocity curve is up to 21%. For NGC 4649, the confidence ranges overlap from 7 kpc outwards and the circular velocity curves agree very well outside 10 kpc. Within this radius the X-ray circular velocity curve is at worst about 21% lower than that of the dynamical model. In NGC 5846, the X-ray circular velocity curve is up to 18% lower in the central 12 kpc than the dynamical circular velocity curve but then rises much more steeply compared to the dynamical circular velocity curve.

6.2.1 Uncertainties in the X-ray analysis

Here we discuss uncertainties in the X-ray analysis, which could explain the discrepancies we observe between the dynamical and X-ray circular velocity curves.

One subject discussed in Churazov et al. (2010) is the contribution of non-thermal components in the gas to the total pressure. The existence of these components would lead to a systematic bias in our determination of the mass profile derived from hydrostatic equilibrium as we have only considered the thermal gas pressure. Churazov et al. (2008) listed several non-thermal components that are consistent with AGN-heated cores of X-ray bright elliptical galaxies exhibiting properties of a cooling flow region: (i) Cosmic rays and magnetic fields uniformly mixed with the thermal gas, (ii) cosmic rays and magnetic fields forming bubbles that are free of thermal gas and (iii) microturbulence in the thermal

gas. If the fraction of the total pressure that is due to thermal gas f_t is constant with radius, then $\phi_t = f_t \phi_{\text{true}}$, where ϕ_t is the potential calculated from the thermal pressure and ϕ_{true} is the true potential. This translates to $f_t = V_{c,t}^2 / V_{c,\text{true}}^2$. As $0 \leq f_t \leq 1$, non-thermal contributions to the pressure are a possible mechanism for lowering the circular velocity curve calculated from the X-rays and therefore could explain the discrepancies we see in NGC 1399, NGC 4472, NGC 4649 and NGC 5846 in the central ~ 10 kpc and throughout NGC 4486. Calculating f_t (for $r > 1$ kpc) where the X-ray circular velocity curve is lowest compared to the dynamical circular velocity curve gives upper limits on the local contribution of non-thermal components to the total pressure of 30%, 45%, 69%, 32% and 33% in NGC 1399, NGC 4472, NGC 4649 and NGC 5846. These local, inner values are higher than those quoted in Churazov et al. (2010), where the f_t is a global estimate from fits to the total potential.

Another possible source of discrepancy could be in the assumptions made about the abundance profile in the determination of deprojected temperature and density profiles. Churazov et al. (2010) assumed a flat abundance profile for their analysis but calculated the average effect on the circular velocity curves if this assumption was relaxed. They found that the circular velocity values generally increase for their sample by a value of $\sim 2\%$. This small effect is in agreement with Werner et al. (2009), who combined very high-resolution XMM Newton data with Chandra data in NGC 4636 and concluded that allowing for a varying abundance

profile does not change the derived deprojected temperature and density profiles significantly. Churazov et al. (2010) also considered the effect of the unresolved population of low-mass X-ray binaries and estimated that this generally lowers the circular velocity curve by $\sim 2\%$, which to some extent counteracts the effect of allowing an abundance gradient.

We also consider the effect of the extrapolation in the deprojection of the spectra on the derived circular velocity profiles. The deprojected density profiles presented in Churazov et al. (2010) and in Figure 1 in this paper assume a power-law extrapolation based on a power-law fit to the data. We consider two alternative extrapolations of the Chandra density profile of NGC 4472, to investigate whether we can explain the discrepancy between the X-ray and dynamical circular velocity curves outside ~ 11 kpc. If the index of the power law used in the extrapolation of the density profiles becomes less negative by 0.1 (i.e. the density profile becomes more shallow), the outermost Chandra circular velocity point decreases by about 10 km/s, and effects further in are not discernable. Therefore this is not a realistic explanation for the discrepancy we observe. If instead the power-law index becomes more negative by 0.1 (i.e. density profile drops off more steeply), then the effect is to increase the circular velocity of the last two Chandra circular velocity points by $\lesssim 10$ km/s. The effects further in are negligible. This would not be sufficient to explain why the X-ray circular velocity curve is so much higher in NGC 1407 compared to the dynamical circular velocity curve.

Shocks in the gas result in a local violation of hydrostatic equilibrium and in spatial correlations in the pressure and circular velocity curves (Section 5.1). In NGC 4486, Churazov et al. (2008) showed a simulated shock at 2.7 arcmin (~ 13 kpc), which could correspond to the acute bump seen in the pressure and temperature profiles around this radius in Figure 6. They found that such a shock leads to a dip in the potential of NGC 4486. We observe a similar dip in the total circular velocity of NGC 4486 close to this radius. In the other galaxies, shockfronts are not obvious in the deprojected profiles, possibly due to the lower statistics compared to NGC 4486. In general, small-scale deviations from hydrostatic equilibrium are simply not fit due to the smoothing prior in our method, while a larger-scale violation results in a systematic effect.

Churazov et al. (2010) also discussed the effects of assuming spherical symmetry in their determination of the gravitational potential from X-rays and found that on average the effect is unlikely to exceed 7%. As the effect is systematic and will either increase/decrease the average slope of the potential, the resulting change in the circular velocity is of the order of 4%.

In earlier work, Churazov et al. (2008) estimated biases introduced when fitting multi-temperature plasma with a single-temperature model by comparing profiles obtained in different energy bands. In the case of NGC 4486, they compared temperature and density profiles calculated from broad-band spectra to that from hard-band spectra and found that differences are small outside 0.4 arcmin, which is a couple of kpc. Within this region however, AGN activity can result in hot and cool gas structures superposed along the line of sight. NGC 4486 is the most disturbed galaxy in our sample but this source of uncertainty could also explain

some of the discrepancies we find in the central few kpc in other galaxies in the sample.

6.2.2 Uncertainties in the dynamical modelling

Here we examine uncertainties associated with the dynamical modelling methods, which could be the source for some of the discrepancies we observe between the dynamical and X-ray circular velocity curves.

In the dynamical models of Kronawitter et al. (2000), the data used extends only to 5–10 kpc. However in the X-ray bright elliptical galaxies in our sample, the density profiles of the stars are shallow in the outer parts, which implies that there is a lot of stellar mass at large radii where the orbital structure remains poorly constrained. If additionally the orbital structure of these outer stars were very radial, as in the numerical simulations of Abadi et al. (2006) and the dynamical models of de Lorenzi et al. (2008, 2009) ($\beta = 1 - \sigma_t^2/\sigma_r^2 \sim 0.5$), there would be many stars on highly elliptical orbits traversing large distances in the galaxy. In the central regions they turn around and contribute to the LOS velocity dispersion more than compared to if they were on a circular orbit there. Therefore a higher mass profile could be inferred in the central region, compared to what would be inferred if the outer kinematics are also available. To estimate how much extra mass may be inferred in the central region we look at the axisymmetric Schwarzschild models of Coma elliptical galaxies in Thomas et al. (2007). They used kinematic data extending to between 13–30 kpc, further out than for the dynamical models in Kronawitter et al. (2000), and provide 68% confidence ranges on their circular velocity profiles. Without the outer kinematics, they would have inferred a less massive dark matter halo, and therefore a higher central stellar mass-to-light ratio. Let us assume that this is approximately given by the upper boundary of the confidence range on the mass profiles in the central region. Therefore the inner mass profile would be overestimated by about 50 km/s without the outer kinematic data, which is about 10% of the circular velocities we obtain from the X-rays. Therefore it could partly but not wholly explain the discrepancies in regions where the dynamical circular velocity curves are higher than the X-ray circular velocity curves.

A similar argument is relevant in cases where the dynamical models do not have central kinematic constraints on the orbital structure, such as in NGC 1407, where only globular cluster kinematics were used from 15 kpc outwards. Central kinematic constraints are invaluable as they are usually of much higher quality than kinematic data further out. In radially anisotropic systems in particular, they not only place stringent constraints on the central dynamical structure, but also constrain the orbital structure at least out to a few times their maximum projected radius.

An assumption on the symmetry of the stellar distribution in the dynamical models can also lead to a systematic bias. Let us consider the case where the stellar distribution is assumed to be spherical but in reality is prolate axisymmetric along the line-of-sight (LOS). Let us position the LOS along the z -axis, which will then be aligned with the long axis of the prolate ellipsoid. Therefore the velocity dispersion along the LOS is higher than in the plane of the sky. As we are measuring only the LOS velocity dispersions, a spherical dynamical model would overestimate the average 3-D

velocity dispersion (σ_{3D}) and therefore also the mass and circular velocity. For an isotropic velocity dispersion tensor, $\sigma_{3D,sp} \approx \sqrt{3}\sigma_{zz}$. If the stellar mass distribution is in fact prolate along the LOS, then $\sigma_{3D,pr} = (2\sigma_{xx}^2 + \sigma_{zz}^2)^{\frac{1}{2}}$, where x and y are along the short axes and $\sigma_{xx} = \sigma_{yy}$ because of axisymmetry. The *Tensor Virial Theorem* relates the intrinsic axial ratios of the stellar mass distribution to its rotation and the anisotropy of the velocity dispersion tensor. Assuming no rotation in this galaxy gives $\sigma_{3D,pr} \approx \sigma_{zz}(1 + 2q^{0.9})^{\frac{1}{2}}$ (e.g. Gerhard 1994), where q is the intrinsic flattening. Therefore $V_{c,true}^2/V_c^2 \approx \sigma_{3D,pr}^2/\sigma_{3D,sh}^2 \approx (1 + 2q^{0.9})/3$. This estimate does not take into account that dynamical models created assuming different shapes for the galaxies may prefer different orbit distributions, which influence the χ^2 minimisation usually employed. Nevertheless, it is a useful way for us to determine approximately how prolate a galaxy has to be along the LOS to explain the discrepancies we observe. Looking at the radii where the dynamical and X-ray circular velocity curves of NGC 1399, NGC 4472, NGC 4486, NGC 4649 and NGC 5846 are most discrepant, we find that for $r > 1$ kpc, maximum flattenings of $q = 0.52, 0.29, 0.14, 0.48, 0.47$ respectively would be required. Tremblay & Merritt (1996) found that the distribution of intrinsic, short-to-long axis ratios peaks at around 0.75 for bright elliptical galaxies. Therefore it is unlikely that prolate axisymmetry along the LOS is the cause for the observed discrepancies.

Finally, the mass profiles explored in the dynamical models are parameterised so that that stellar mass contribution follows the shape of the stellar luminosity profile (i.e. the mass-to-light ratio is constant with radius). The dark matter mass contribution is usually given by non-singular isothermal spheres or NFW profiles. This results in a bias in the shape of the mass profiles and circular velocity curves, especially noticeable in the central regions where the shape of the circular velocity profile changes most.

Based on our discussion on the uncertainties inherent in the derivation of circular velocity curves from X-rays and from dynamical models, we conclude that the regions where the X-ray circular velocity curves are lower compared to dynamical circular velocity curves in NGC 1399, NGC 4472 and NGC 5846 can probably be attributed to a combination of: i) A contribution of non-thermal components to the pressure in the X-rays, ii) multiple-temperature components in the gas, iii) an incomplete spatial coverage in the kinematic data used in the dynamical models, and iv) insufficiently general mass profiles in the dynamical modelling. As the dynamical models for NGC 4486 and NGC 4649 incorporate extended kinematic data, the probable explanation is: i) the existence of non-thermal pressure components, ii) multiple-temperature components, and iii) insufficiently general mass profiles in the dynamical models only. The discrepancy between the X-ray and dynamical circular velocity curves in NGC 1407 remains unclear.

6.3 How non-isothermal are the mass profiles?

In the previous section we carried out an individual comparison between the circular velocity curves we obtained to those obtained in the literature. Here we examine the general property of rising circular velocity curves noted in Section 5.1.

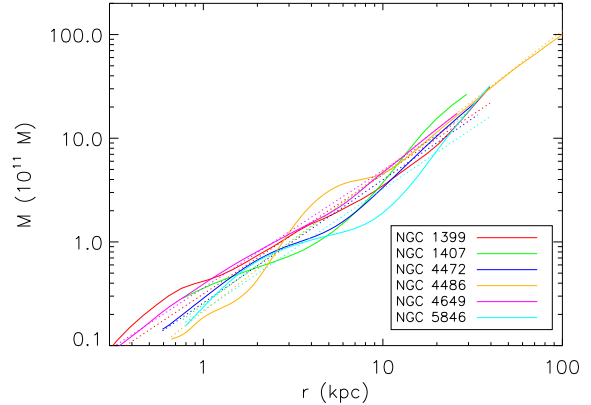


Figure 10. The non-isothermality of the mass profiles of the sample of six X-ray bright elliptical galaxies: Solid lines show the mass distributions in a double-logarithmic scale. Dotted lines show straight lines fitted to the mass distributions in this scale.

To quantify how non-isothermal the circular velocity curves are, we fit a power-law model $M \propto r^\zeta$ to the mass profiles as done by Fukazawa et al. (2006) and Humphrey et al. (2009) from their analysis of XMM-Newton and Chandra observations, and Churazov et al. (2010) on the sample we work with. Our determinations of ζ are listed in columns (6)–(8), calculated by fitting to the total mass profile, the mass profile within 10 kpc and the mass profile outside 10 kpc. Figure 10 shows the mass profiles in a log-log scale with the best-fit models fit over the whole radial range. In this plot, the slope of the best-fit lines is equal to the power-law index ζ . For a galaxy with an isothermal mass profile, we would expect $\zeta = 1$. Fitting to the the total mass profile we find $1.13 < \zeta < 1.36$ and a mean $\langle \zeta \rangle = 1.21$. As the $1\text{-}\sigma$ errors range between 0.01 and 0.07, the sample of these six elliptical galaxies appear to have significantly non-isothermal mass profiles. Fitting the mass profiles within 10 kpc, we find $0.88 < \zeta < 1.60$ and a mean $\langle \zeta \rangle = 1.10$. For NGC 1399, ζ does not change, for NGC 4486, ζ becomes much larger, possibly due to the shockfront at this radius, but for the remaining galaxies ζ decreases to values between 0.88 and 1.08. Calculating ζ from the mass profiles outside 10 kpc, we find higher values ranging from $1.26 < \zeta < 2.16$ and a mean $\langle \zeta \rangle = 1.56$. This implies that the central 10 kpc of these galaxies may be isothermal, but outside this radius the circular velocity curves are rising. The rising circular velocity curves could be showing that we have probed the mass distribution sufficiently far out to observe the effects of the massive group/cluster-sized haloes in which these galaxies reside.

Fukazawa et al. (2006) obtained mass profiles by applying hydrostatic equilibrium to parametrised Chandra and XMM-Newton temperature and density profiles for a sample of 53 elliptical galaxies. They fit power-law mass models outside 10 kpc, finding on average $\zeta = 1.33 \pm 0.33$, which overlaps with our determination of 1.56.

Churazov et al. (2010) found a mean $\langle \zeta \rangle = 1.11$ for NGC 1399, NGC 4472, NGC 4486, NGC 4649 and NGC 5846, fitting their potentials between 0.1' and 5'. Over the

same radial range for the same galaxies, we obtain $\langle \zeta \rangle = 1.17$, which is only $\sim 5\%$ higher.

Humphrey & Buote (2010) derived mass profiles from a parametric Bayesian analysis of Chandra observations for a sample of 10 galaxies, groups and clusters. They obtained $0.95 < \zeta < 1.8$ fitting to the mass profiles between $0.2\text{--}10R_e$ but for the four galaxies in their sample, they obtained $0.95 < \zeta < 1.09$, i.e., close to isothermal. We believe that the differences between their results and ours is due to: i) Calculation of ζ over different radial ranges from ours and ii) environmental effects, i.e. our galaxies are located specifically at the centre of sub-groups, groups or clusters while their galaxies, though belonging to similar environments, are generally not at the centre. The radial range is important in the case of NGC 4649, the only galaxy common to both samples. They used data until about ~ 17 kpc, converted to our assumed distance. If we look at Figure 1 we can see that there is an extra deprojected temperature and density point that we have from the XMM-Newton analysis, which increases the gradient of the mass profile. There is also reason to believe this increase because of how similar our derived circular velocity curve is to that from Shen & Gebhardt (2010) discussed in Section 6.2. For NGC 1332 Humphrey & Buote (2010) used data only until ~ 20 kpc, which also may not be sufficiently extended (our profiles all extend to at least ~ 25 kpc and in the case of NGC 4486, until almost 110 kpc.) NGC 720, NGC 4261 (for which they have data until ~ 31 and ~ 34 kpc) and NGC 1332 are not located at the centre of their respective environments. Therefore even if the profiles were as radially extended as ours, we would not expect the circular velocity curves to rise as much as for our sample galaxies, which are all located at the centre of their environments. For the groups and clusters in the sample of Humphrey & Buote (2010), they found mass profiles that increase more steeply than isothermal mass profiles, therefore supporting the hypothesis that we are partially probing the region where the group/cluster potentials start dominating. The comparison between calculating ζ within 10 kpc with calculating it over the whole radial range of the deprojected temperature and density profiles also supports this hypothesis.

Gerhard et al. (2001) analysed the dynamical models of Kronawitter et al. (2000) and found that their circular velocity curves are flat to within 10% for $R \gtrsim 0.2R_e$. These models use photometric and kinematic data extending to less than $1R_e$ for 9/21 of the galaxies, between $1\text{--}2R_e$ for 6/21 of the galaxies and $2\text{--}3R_e$ for 6/21 of the galaxies. Koopmans et al. (2009) solved constant-anisotropy spherical Jeans equations for 58 strong-lens early type galaxies using stellar velocity dispersion constraints and lensing-based total masses within the central effective radius. They found an average logarithmic mass-density slope of -2.085 (for an isothermal mass profile, one would expect -2.0) and that the dependence of this result on the value of the anisotropy parameter β is small. Both studies used elliptical galaxies that cover a range of luminosities and are not constrained to reside at the centre of sub-group/group/cluster environments. This means that for many of their galaxies, we have no reason to expect a rising circular velocity curve and for those that we do, the mass profiles may not be probing far out enough and/or the lack of extended photometric and kinematic constraints could be biasing the inner mass profile as discussed in Section 6.2.2.

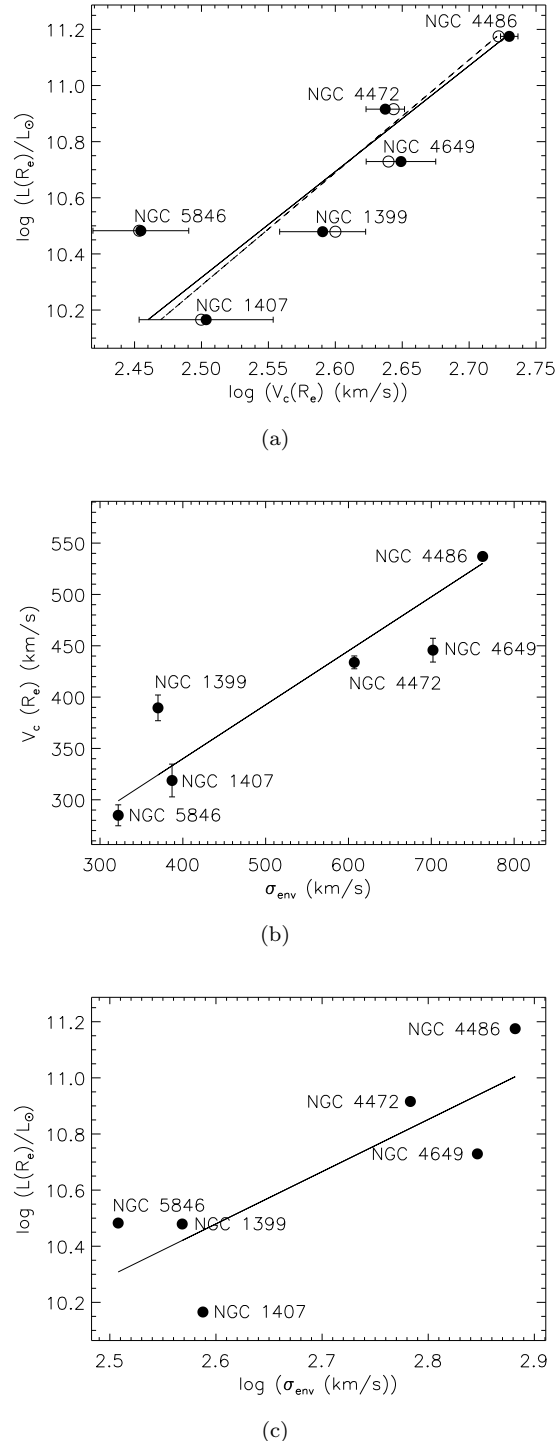


Figure 11. Correlations between the stellar component, the total circular velocity, and the environment: (a) Tully-Fisher relation between the luminosity of the stellar component at $1R_e$ and the total circular velocity from the X-rays at $1R_e$ (black filled circles) and associated 95% confidence range (horizontal bars). Also shown are the results of considering the average effect of the unresolved population of low-mass X-ray binaries and an abundance gradient (black open circles). (b) Total circular velocity from X-rays at $1R_e$ and the velocity dispersion of the environment (black filled circles). (c) Luminosity of the stellar component at $1R_e$ against the velocity dispersion of the environment (black filled circles). Solid black and dashed black lines show straight-line fits to the black filled circles and open circles respectively.

6.4 Correlations between the total circular velocity curves, the stellar component and the environment

The Tully-Fisher relation links the luminous component to the total mass of the galaxies and for spiral galaxies is usually shown between the total luminosity and the flat part of the circular velocity curve. We plot an analogous relation for our sample between the total B -band luminosity at R_e against the total circular velocity from the X-rays at R_e , shown with black filled circles in Figure 11. We have also plotted with black open circles, the approximate total circular velocities at these radii if we take into account the average effects of the unresolved population of low-mass X-ray binaries and varying abundance profiles, as estimated by Churazov et al. (2010). The solid black and dashed black lines show straight lines fit to the black filled circles and black open circles respectively, considering the errors in the circular velocity. The lines have slopes of 3.77 ± 0.03 and 4.01 ± 0.03 , very similar to the value of 4 in the Tully-Fisher relation for spiral galaxies and to the value of ~ 4 (*private communication* with J. Thomas) obtained for the sample of Coma cluster elliptical galaxies analysed in Thomas et al. (2009). PMCC values for the fits are 0.86 and 0.85, therefore supporting a linear correlation at a $\sim 95\%$ level of significance for a sample size of six. This implies that systems with more luminous stellar components tend to have higher circular velocities.

Figure 11(b) shows the relation between the circular velocity at R_e and the velocity dispersion of the surrounding environment from column (6) in Table 1. The solid line shows the best-fit straight line with a slope of 0.53 ± 0.02 and a PMCC value of 0.92, supporting a linear correlation at a 98% level of significance. This strongly implies that central galaxies residing in hotter environments (as measured by the velocity dispersions) have higher circular velocities. Figure 11(c) shows the logarithm of the luminosity at R_e against the logarithm of the velocity dispersion of the surrounding environment. The best-fit straight line has a PMCC value of 0.83, supporting a linear correlation at a level of $\sim 95\%$ significance. This implies that the luminosity of the galaxy residing at the centre of a sub-clump, group or cluster environment, is related to the velocity dispersion of the environment.

In environments where the local velocity dispersions are higher, the densities ($\sim \sigma^2/r^2$) are also greater, as the radii (0.7–1 Mpc) over which these velocity dispersions were calculated are comparable. Therefore one would expect that a larger number of systems would fall onto the central galaxy, resulting in a more luminous stellar component and a more massive dark matter halo. Brough et al. (2007) found that more X-ray luminous systems are intrinsically brighter in the K -band compared to less luminous X-ray luminous systems for their sample of three brightest group galaxies and three brightest cluster galaxies. In denser environments, one would expect the gas to be hotter and denser, and therefore more X-ray luminous, thereby corroborating the results of Brough et al. (2007).

7 CONCLUSIONS

In this paper, we describe a new non-parametric Bayesian approach to obtain mass distributions and associated confidence ranges from temperature and density profiles of hot gas in hydrostatic equilibrium. The method is able to successfully reconstruct the mass distribution of a test galaxy just within a 68% confidence range of the recovered models. We assume a smoothing prior to ensure unique and physical mass distributions and calibrate this on the test galaxy.

We apply the procedure to the sample of six X-ray bright elliptical galaxies from Churazov et al. (2010), who used high-quality X-ray observations of Chandra and XMM-Newton to obtain temperature and density profiles of the hot gas. We find total mass distributions with an average mass of $\sim 1.5 \times 10^{12} M_\odot$ and average circular velocity of ~ 515 km/s at a radius of 25 kpc.

The total circular velocity curves of our sample are all rising in the outer parts as a result of both an increasing temperature profile and a logarithmic pressure gradient that generally increases in magnitude outwards. Therefore the mass distributions of our sample are not isothermal, suggesting that we are probing the mass distribution sufficiently far out to observe the effects of the massive group/cluster haloes in which these galaxies reside. Increasing circular velocity curves appear to contradict work done in the past but are most likely a consequence of: i) Samples in the literature not restricted to only massive elliptical galaxies and/or ii) mass profiles not being probed sufficiently far out.

The stellar components of our sample show a remarkable coherence in their surface-brightness profiles when scaled by the radius where $d\mu/d\log R = 2$. We find however that the effective radius is a better proxy for the luminosity of the stellar component. The dark matter mass fraction is 35–80% at $2R_e$ and increases to about 80–90% at the outermost radii.

Except in the case of NGC 1407, our determination of circular velocity curves from X-rays agrees well with previous X-ray determinations. When comparing our circular velocity curves with those found by dynamical models in the literature, we find that the X-ray circular velocity curves are often lower, particularly in the central 10 kpc. This is probably due to contributions from: i) Non-thermal pressures, ii) multiple-temperature components, iii) incomplete spatial coverage in the kinematic data used for the dynamical models, and iv) insufficiently general mass profiles explored in the dynamical modelling.

Looking at relations between the luminosity of the stellar component at R_e , the total circular velocity at R_e and the velocity dispersion of the environment, we find evidence for a dependence of the properties of central galaxies on their environment.

The next steps in this project are to extend the analysis to a larger sample of X-ray bright elliptical galaxies to examine the isothermality of their circular velocity curves, and to obtain more stringent constraints on how they compare with alternative methods of mass determinations, in particular through the construction of more radially extended dynamical models. This will enable us to build up a clearer picture of the connection between properties of central X-ray bright elliptical galaxies and the environment in which they reside.

ACKNOWLEDGEMENTS

PD was supported by the DFG Cluster of Excellence “Origin and Structure of the Universe”. EC and IZ were supported by the DFG grant CH389/3-2 and OFN-17 program of the Russian Academy of Sciences. PD and IZ would like to thank the International Max Planck Research School (IMPRS) in Garching.

REFERENCES

- Abadi M. G., Navarro J. F., Steinmetz M., 2006, *MNRAS*, 365, 747
- Bender R., Döbereiner S., Möllenhoff C., 1988, *A&AS*, 74, 385
- Brough S., Proctor R., Forbes D. A., Couch W. J., Collins C. A., Burke D. J., Mann R. G., 2007, *MNRAS*, 378, 1507
- Caon N., Capaccioli M., D’Onofrio M., 1994, *A&AS*, 106, 199
- Cappellari M., Bacon R., Bureau M., Damen M. C., Davies R. L., de Zeeuw P. T., Emsellem E., Falcón-Barroso J., Krajnović D., Kuntschner H., McDermid R. M., Peletier R. F., Sarzi M., van den Bosch R. C. E., van de Ven G., 2006, *MNRAS*, 366, 1126
- Churazov E., Forman W., Jones C., Böhringer H., 2003, *ApJ*, 590, 225
- Churazov E., Forman W., Vikhlinin A., Tremaine S., Gerhard O., Jones C., 2008, *MNRAS*, 388, 1062
- Churazov E., Tremaine S., Forman W., Gerhard O., Das P., Vikhlinin A., Jones C., Böhringer H., Gebhardt K., 2010, *MNRAS*, 404, 1165
- Cowie L. L., Henriksen M., Mushotzky R., 1987, *ApJ*, 317, 593
- de Lorenzi F., Gerhard O., Coccato L., Arnaboldi M., Capaccioli M., Douglas N. G., Freeman K. C., Kuijken K., Merrifield M. R., Napolitano N. R., Noordermeer E., Romanowsky A. J., Debattista V. P., 2009, *MNRAS*, 395, 76
- de Lorenzi F., Gerhard O., Saglia R. P., Sambhus N., Debattista V. P., Pannella M., Méndez R. H., 2008, *MNRAS*, 385, 1729
- Dejonghe H., de Bruyne V., Vauterin P., Zeilinger W. W., 1996, *A&A*, 306, 363
- Drinkwater M. J., Gregg M. D., Colless M., 2001, *ApJ*, 548, L139
- Faber S. M., Wegner G., Burstein D., Davies R. L., Dressler A., Lynden-Bell D., Terlevich R. J., 1989, *ApJS*, 69, 763
- Forman W., Jones C., Churazov E., Markevitch M., Nulsen P., Vikhlinin A., Begelman M., Böhringer H., Eilek J., Heinz S., Kraft R., Owen F., Pahre M., 2007, *ApJ*, 665, 1057
- Fukazawa Y., Botoya-Nonesá J. G., Pu J., Ohto A., Kawano N., 2006, *ApJ*, 636, 698
- Gavazzi G., Boselli A., Scodreggio M., Pierini D., Belsole E., 1999, *MNRAS*, 304, 595
- Gavazzi R., Treu T., Rhodes J. D., Koopmans L. V. E., Bolton A. S., Burles S., Massey R. J., Moustakas L. A., 2007, *ApJ*, 667, 176
- Gebhardt K., Richstone D., Tremaine S., Lauer T. R., Bender R., Bower G., Dressler A., Faber S. M., Filippenko A. V., Green R., Grillmair C., Ho L. C., Kormendy J., Magorrian J., Pinkney J., 2003, *ApJ*, 583, 92
- Gebhardt K., Thomas J., 2009, *ApJ*, 700, 1690
- Gerhard O., Jeske G., Saglia R. P., Bender R., 1998, *MNRAS*, 295, 197
- Gerhard O., Kronawitter A., Saglia R. P., Bender R., 2001, *AJ*, 121, 1936
- Gerhard O. E., 1994, in G. Contopoulos, N. K. Spyrou, & L. Vlahos ed., *Galactic Dynamics and N-Body Simulations Vol. 433 of Lecture Notes in Physics*, Berlin Springer Verlag, Elliptical galaxies. pp 191–274
- Hopkins P. F., Cox T. J., Dutta S. N., Hernquist L., Kormendy J., Lauer T. R., 2009, *ApJS*, 181, 135
- Humphrey P. J., Buote D. A., 2010, *MNRAS*, 403, 2143
- Humphrey P. J., Buote D. A., Brighenti F., Gebhardt K., Mathews W. G., 2008, *ApJ*, 683, 161
- Humphrey P. J., Buote D. A., Brighenti F., Gebhardt K., Mathews W. G., 2009, *ApJ*, 703, 1257
- Humphrey P. J., Buote D. A., Gastaldello F., Zappacosta L., Bullock J. S., Brighenti F., Mathews W. G., 2006, *ApJ*, 646, 899
- Koopmans L. V. E., Bolton A., Treu T., Czoske O., Auger M. W., Barnabè M., Vegetti S., Gavazzi R., Moustakas L. A., Burles S., 2009, *ApJ*, 703, L51
- Kormendy J., 1977, *ApJ*, 218, 333
- Kormendy J., Fisher D. B., Cornell M. E., Bender R., 2009, *ApJS*, 182, 216
- Kronawitter A., Saglia R. P., Gerhard O., Bender R., 2000, *A&AS*, 144, 53
- Lauer T. R., Gebhardt K., Faber S. M., Richstone D., Tremaine S., Kormendy J., Aller M. C., Bender R., Dressler A., Filippenko A. V., Green R., Ho L. C., 2007, *ApJ*, 664, 226
- Liddle A. R., 2009, *Annual Review of Nuclear and Particle Science*, 59, 95
- Magorrian J., 1999, *MNRAS*, 302, 530
- Mahdavi A., Trentham N., Tully R. B., 2005, *AJ*, 130, 1502
- Mandelbaum R., Seljak U., Cool R. J., Blanton M., Hirata C. M., Brinkmann J., 2006, *MNRAS*, 372, 758
- Matsushita K., Belsole E., Finoguenov A., Böhringer H., 2002, *A&A*, 386, 77
- Merritt D., Tremblay B., 1994, *AJ*, 108, 514
- Naab T., Johansson P. H., Ostriker J. P., 2009, *ApJ*, 699, L178
- Nagino R., Matsushita K., 2009, *A&A*, 501, 157
- Nulsen P. E. J., Böhringer H., 1995, *MNRAS*, 274, 1093
- O’Sullivan E., Forbes D. A., Ponman T. J., 2001, *MNRAS*, 328, 461
- Rix H., de Zeeuw P. T., Cretton N., van der Marel R. P., Carollo C. M., 1997, *ApJ*, 488, 702
- Romanowsky A. J., Strader J., Spitler L. R., Johnson R., Brodie J. P., Forbes D. A., Ponman T., 2009, *AJ*, 137, 4956
- Saglia R. P., Kronawitter A., Gerhard O., Bender R., 2000, *AJ*, 119, 153
- Shen J., Gebhardt K., 2010, *ApJ*, 711, 484
- Spolaor M., Forbes D. A., Hau G. K. T., Proctor R. N., Brough S., 2008, *MNRAS*, 385, 667
- Thomas J., Saglia R. P., Bender R., Thomas D., Gebhardt K., Magorrian J., Corsini E. M., Wegner G., 2007, *MNRAS*, 382, 657
- Thomas J., Saglia R. P., Bender R., Thomas D., Gebhardt K., Magorrian J., Corsini E. M., Wegner G., 2009, *ApJ*, 691, 770

- Thomas J., Saglia R. P., Bender R., Thomas D., Gebhardt K., Magorrian J., Richstone D., 2004, MNRAS, 353, 391
- Tonry J. L., Dressler A., Blakeslee J. P., Ajhar E. A., Fletcher A. B., Luppino G. A., Metzger M. R., Moore C. B., 2001, ApJ, 546, 681
- Trager S. C., Faber S. M., Worthey G., González J. J., 2000, AJ, 120, 165
- Tremblay B., Merritt D., 1996, AJ, 111, 2243
- Trentham N., Tully R. B., Mahdavi A., 2006, MNRAS, 369, 1375
- Treu T., Koopmans L. V. E., 2004, ApJ, 611, 739
- van Dokkum P. G., Franx M., Kriek M., Holden B., Illingworth G. D., Magee D., Bouwens R., Marchesini D., Quadri R., Rudnick G., Taylor E. N., Toft S., 2008, ApJ, 677, L5
- Werner N., Zhuravleva I., Churazov E., Simionescu A., Allen S. W., Forman W., Jones C., Kaastra J. S., 2009, MNRAS, 398, 23
- Zhang Z., Xu H., Wang Y., An T., Xu Y., Wu X., 2007, ApJ, 656, 805